

FLUID MIGRATION DURING ICE/ROCK PLANETESIMAL DIFFERENTIATION

A Thesis

By

ROBERT DYLAN RANEY

Submitted to the Office of Graduate Studies of
Texas A&M University
in partial fulfillment of the requirements for the degree of

MASTER OF SCIENCE

Approved by:

Chair of Committee,	David Sparks
Committee Members,	Mike Tice
	Mark T. Lemmon
Head of Department,	Rick Giardino

December 2012

Major Subject: Geophysics

Copyright 2012 Robert Dylan Raney

ABSTRACT

Much speculation on extraterrestrial life has focused on finding environments where water is present. Heating of smaller icy bodies may create and sustain a possible liquid layer below the surface. If liquid water was sustained for geologically significant times ($> 10^8$ years) within the ubiquitous small bodies in the outer solar system, the opportunities for development of simple life are much greater. The lifetime of the liquid water layer will depend on several factors, including the rate of rock/water reaction, which will depend on the rate at which water can be segregated from a melting ice/rock core. For the liquid water phase to migrate toward the surface, the denser rock phase must compact. The primary question that this thesis will answer is how fast melt water can segregate from the core of an ice-rich planetesimal.

To answer this question we treat the core as two phase flow problem: a compacting viscous “solid” (ice/rock mixture) and a segregating liquid (melt water). The model developed here is based on the approach derived to study a different partially molten solid: in the viscously deforming partially molten upper mantle. We model a planetesimal core that initially a uniform equal mixture of solid ice and rock. We assume chondritic levels of radiogenic heating as the only heat source, and numerically solve for the evolution of solid and melt velocities and the distribution of melt fraction (“porosity”) during the first few million years after accretion. From a suite of numerical models, we have determined that the meltwater is segregated out of the core as fast as it is created, except in the case of very fast melting times (0.75 My vs. 0.62 My), and small

core radius (~25 to 150 km, depending on the viscosity of the ice/rock mixture in the solid core). In these latter cases, segregation is slower than migration and a high water fraction develops in the core. Heat released by water-rock reactions (not included in this model) will tend to drive up melting rates in all cases, which may favor this latter endmember.

TABLE OF CONTENTS

	Page
ABSTRACT.	ii
TABLE OF CONTENTS.	iv
LIST OF FIGURESvi
LIST OF TABLES.ix
1. INTRODUCTION.	1
2. THE PHYSICS OF MELTING AND DIFFERENTIATING BODIES.	6
2.1 Thermal History of an Icy Planetesimal.6
2.2 Compaction and Fluid Migration.	9
2.3 Melting and Compaction in a Planetesimal Core.	18
3. THE GOVERNING EQUATIONS OF COMPACTION.	24
3.1 Compaction Equations in Cartesian Coordinates.	24
3.2 Compaction Equations in Spherical Core.	29
3.3 Scaling of Spherical Compaction Equations.32
3.4 Numerical Solution.35
4. SPHERICAL VS. CARTESIAN COMPARISON, NO MELTING.	37
5. RESULTS FOR MELTING PLANETESIMALS.	43
5.1 Endmember 1: Melting Faster than Migration.44
5.2 Endmember 2: Melting Slower than Migration.	50
5.3 Effect of Melting Rate and Size of Core.56
6. DISCUSSION.63
6.1 Large h Approximation.65
6.2 Timing of Melting and Segregation.	67

7. CONCLUSION.	71
REFERENCES.	74
APPENDIX 1.	77

LIST OF FIGURES

FIGURE		Page
1.	The system as it appears at the beginning of melting and after the completion of segregation.	8
2.	Schematic diagram of the evolution of porosity vs. height in a 1-D column with an initially small and uniform porosity (blue line). This is based on the problem solved in Richter & McKenzie (1984), and solved in Section 5.	11
3.	Mixture Viscosity from Eq. (2) scaled by the viscosity of the pure system as a function of rock fraction, for three choices of the empirical parameter β	14
4.	Compaction length vs. rock fraction from Eq. (3), where the solid viscosity is given by Eq. (2) with three different values of the parameter β . The permeability is taken to be 10^{-15} m^2 , and the fluid viscosity is $10^{-3} \text{ Pa}\cdot\text{s}$	15
5.	A contour map of h values (core radius/compaction length) as a function of core radius and viscosity ratio. The compaction length assumes a core permeability of $8 \times 10^{-15} \text{ m}^2$	17
6.	Melting rate vs. the time of accretion for a planetesimal. The consultants which we have used in the previously described equations were taken from Table 1.	22
7.	Porosity vs. dimensionless height in a non-melting Cartesian System. The separate curves show porosity at ten uniformly spaced times after the initiation of compaction.	38
8.	Dimensionless solid velocity vs. dimensionless height in a non-melting Cartesian System. Note that these velocities are negative because the solid moves downward. The separate curves show porosity at ten uniformly spaced times after the initiation of compaction.. . . .	39
9.	Porosity vs. dimensionless radius in a Spherical system, as in Fig. 7.	40
10.	Dimensionless solid velocity vs. the dimensionless radius in a Spherical system, as in Fig. 8.	41

11. Porosity vs. compaction length with a fast melting value (.86 million years accretion time) and a radius of five compaction lengths. The separate curves show porosity at different dimensionless times..	44
12. Velocity of solid phase vs. height for the compacting Spherical model shown in Fig. 11..	45
13. The evolution of the radius of the top of the melting core, scaled by the original size of the core, vs. time for the run with $h = 5$ and $\Gamma' = 4.46 \times 10^{-11}$. The break in slope, at which time almost all of the melt has segregated from the core, is the “end of compaction”..	47
14. Composition of the melting core (based on volume fraction of ice, rock, and water) vs. time at the center of the core ($r = 0$) for the simulation shown in Fig. 11 & 12. The area below the red curve represents the volume fraction of ice, and the area above the blue curve is the volume fraction of water. The area between the two separate curves represents the volume fraction of rock..	48
15. Composition of the melting core (based on volume fraction of ice, rock, and water) vs. time at mid-radius ($r = \frac{r_c}{2}$) for the simulation shown in Fig. 11 & 12. See Fig. 14 for an explanation of curves.	49
16. Porosity vs. compaction length with a slow melting value (6.71 million years accretion time) and a melting core with a radius of five compaction lengths. Note that the time intervals between curves is much longer than in Fig. 10..	51
17. Velocity of the solid matrix vs. the dimensionless radius for the compacting Spherical model from Fig. 16..	52
18. The evolution of the radius of the top of the melting core, scaled by the original size of the core, vs. time for the run with $h = 5$ and $\Gamma' = 6.23 \times 10^{-13}$. The break in slope, at which time almost all of the melt has segregated from the core, is the “end of compaction”.	53
19. Composition of the melting core (ice, rock, and water) at the center of the planetesimal vs. time for the simulation shown in the Figs. 16 & 17 (melting slower than migration endmember). See Fig. 13 for description. . .	54
20. A close up of the water region of Fig. 19, showing the small increase in the water fraction before it reverts to ~ 0.002 (which we do not allow to be extracted).	54

21. Composition of the melting core (ice, rock, and water) at the $\left(r = \frac{h}{2}\right)$ vs. time for the simulations in Figs. 16 & 17.	55
22. A close up of the water region of Fig. 19, showing the small increase in the water fraction before it reverts to ~ 0.002 (which we do not allow to be extracted).	55
23. A composite of all of the porosity (x-axis) vs. dimensionless radius (y-axis) graphs for 5 different core size, (h) and two melting rates $\Gamma = 4.46 \times 10^{-11} - 6.23 \times 10^{-13}$	57
24. These are the results of the program runs for the composition of the melting core (based on volume fraction of ice, rock, and water) (y-axis) vs. time at the $\left(r = \frac{h}{2}\right)$ (x-axis) for the simulations in Fig. 23.	59
25. The position of the base of the accumulated water layer, R_w , relative to the original radius of the melting core vs. dimensionless time, for all of the fast melting rate simulations.	60
26. The position of the base of the accumulated water layer, R_w , relative to the original radius of the melting core vs. dimensionless time, for the slower melting rate, and a range of core radii.	61
27. Maximum core-averaged porosity (at different sizes of planetesimals) vs. the dimensionless planetesimal radii.	62
28. Dimensionless time for complete melting vs. dimensionless core radius. . . .	63
29. Dimensionless time for core compaction vs. dimensionless core radius. . . .	64
30. Dimensionless time that the maximum core-averaged porosity (Fig. 27) was reached for each run vs. the dimensionless planetesimal radii.	64
31. Melting time $\left(\frac{Kg}{m^3s}\right)$ vs. initial core radius (km). This assumes a ratio of solid viscosity to ice viscosity of 10^6	69
32. Segregation time/Melt time vs. core radius.	69

LIST OF TABLES

TABLE	Page
1. These are the values of each element for the concentration, heat produced, and the combined value at a time of zero million years before accretion. (McCord & Sotan, 2005).	20
2. This table is a listing of variables that we use in the thesis, including the meanings of each variable range of assigned values and the respective units for each.. . . .	23

1. INTRODUCTION

Liquid water appears to be a prerequisite for the development and continued existence of life. For this reason speculation on extraterrestrial life has focused on finding environments where water is present. Because of the components of water (hydrogen and oxygen) it is one of the most abundant compounds in the universe. However liquid water is stable under temperature and pressure conditions that are relatively rare in the solar system, of the other terrestrial planets only Mars and possibly Venus have been determined to have the capability of sustaining liquid water either now or in the distant past. Most of the bodies in the solar system are too small to possess a sustainable atmosphere, and far enough from the sun that their surfaces are too cold to allow surface water. However many smaller planetesimals, comets, & moons in the outer solar system have been determined to possess large amounts of water ice (Johnson 2005), as well as a possible liquid layer below the surface of some of the planetesimals.

The potential for long term heat retention is far greater in larger bodies since the dominant heat source (radioactive decay) is proportional to volume, while heat loss to space is proportional to surface area. Larger planetesimals (> 2000 km diameter) have the potential to create liquid water layers that can last for billions of years. In addition, the etched surfaces of the Galilean satellites Europa and Ganymede represent evidence of tidal forces generated by the gravitational exertions of Jupiter on the satellite, which create a secondary heat source. These two bodies have been shown to currently contain liquid water layer “oceans” hundreds of kilometers beneath their frozen crusts (Gurnett

et. al. 1996, Sohl et al., 2010 & Sohl 2010). There is also some evidence for such ocean layers on other moons such as Titan (Kerr 2012), Enceladus (Choi 2006), Consolmagno (1983) and Callisto (Bennett 2001).

But there are thousands of ice-rich bodies in our solar-system that are considerably smaller than these bodies. The Kuiper belt is the home for the majority of these objects. It remains to be determined just how many objects reside past Neptune's orbit (De Sanctis et.al, 2001 & Merk, R. & Prialnik, D., 2006, 2003), but current estimates are in the hundreds of thousands over the size of 100 km in diameter. If liquid water was sustained within these bodies, the opportunities for development of simple life are much greater. These numerous yet small solar bodies lose internal heat at significantly faster rates than larger bodies; therefore many may be frozen today. But if these planetesimals were able to maintain internal liquid water layers for geologically significant times ($> 10^8$ years), there could have been a great many laboratories of biological evolution.

Models of the thermal evolution of small planetary bodies (Merk and Prialnik, 2006 & Prialnik and Bar-Nun, 1989) show that heating from early radioactive decay causes an increase in internal temperature, leading to melting of the ice phase, followed by a slow cooling and refreezing over time. The duration of the liquid water phase will depend on the size of the body, the amount of radiogenic heat generation, the rate of rock/water reaction, and the radial conductivity and heat production profile, which are determined by the distribution of rock, water and ice phases within the planetesimal. This distribution will change in time as the denser rock phase compacts to form a core,

while the liquid water phase segregates toward the surface. The time scale for this segregation has not been previously addressed; it will depend on the mechanism of segregation and the temporal evolution of material properties.

The primary question that this thesis will answer is how fast melt water can segregate from the core of an ice-rich planetesimal. One end member possibility is very slow segregation which occurs if the permeability is very low, or the solid ice/rock core cannot compact easily. In this case the melt does not flow fast enough to segregate into a water layer before refreezing or chemically reacting with the rock. The other end member is a situation with a high permeability and a solid core that is capable of compacting at a fast rate. This would allow for fast melt flow even when the solid compacts to low porosity. Therefore there would be very little melt fraction present within the melting core since melt would segregate as fast as it forms. In this case, water can be completely removed from the core, to form a trapped water layer (or be lost to space. Another implication of this end member is that the thermal properties of water won't have much effect on the core.

Another aspect of the rate of segregation is its effect on the serpentinization of the rock in the core. The silicate part of low pressure planetesimals is made largely of the ultramafic minerals olivine and pyroxene (Elkins-Tanton et. al., 2011). These minerals are unstable in the presence of liquid water and undergo a chemical reaction to form hydrated minerals such as the various forms of serpentine (Malvoisin et. al., 2012). The reaction between olivine and water is relatively fast, but if the water were to be removed from the system quickly enough it then would have no time to chemically react. This fast

extraction of the liquid would limit serpentinization since the heat released by this exothermal reaction may be a major heat source.

The extent and timing of melt water segregation and serpentinization control the dynamics of the water layer. For this reason, it is important to be able to estimate the time scale of melt segregation. The purpose of this study is to put bounds on the length of time necessary for the segregation of the solid matrix and the ice melt, and to understand what controls the segregation rate.

To estimate the time it takes for the segregation of melt water from the melting ice/rock core we consider a one dimensional problem of two phase flow; a compacting viscous “solid” and a segregating liquid. The model developed here is based on the approach derived to study a different partially molten solid: in the viscously deforming partially molten upper mantle (McKenzie 1984, Richter & McKenzie 1984, & Ribe 1985a). The model development is described in Section 2.

In Section 3, we convert the equations of motion derived in McKenzie’s (1984) equations into a radially-symmetric spherical coordinate system. We also follow the suggestions of Richter & McKenzie (1984) in introducing the “compaction length” as the fundamental length scale that controls the style of migration behavior. We describe a computer program to solve these equations numerically. Section 4 compares the 1-D cartesian problem of Richter and McKenzie to a similar 1-D spherical case in order to highlight the effect of some of the differences from that well-studied problem, primarily the effect of geometric spreading with distance from the core and the variation of the driving gravity force with radius. In Section 5, we describe results from a series of

models in which we vary the key parameters. We identify two key ratios that determine whether the meltwater segregation will be very fast or slow: the size of the melting core of ice relative to the compaction length, and the rate of melting relative to the rate of melt flow. In Section 6 we discuss the implications of these models.

2. THE PHYSICS OF MELTING AND DIFFERENTIATING BODIES

2.1 Thermal History of an Icy Planetesimal

The most widely accepted theory of solar system formation is the Nebular Hypothesis. This hypothesis holds that all bodies of the solar system were formed from a cloud of gas & dust with a composition, similar to that of the Sun. The non-volatile component of this composition is represented today by the chondritic meteorites. Our model of a rock-ice body assumes a chondritic composition of the rock part mixed with a variable amount of water ice (Johnson 2004, McCord & Sotin 2005, Consolmagno & Lewis 1978, Wilson et. al., 1999, & Brush 1977). The ice portion will most likely contain other volatile materials, such as CO₂ and hydrocarbons, as are also found in carbonaceous chondrites. While those materials are crucial for the development of life, they will not affect the energy on momentum balances of our model, and can be neglected. This work aims to provide constraints on the water segregation process in a thermal/chemical model of an icy planetesimal (Farrell et al, 2007). The rest of this section outlines the assumptions of the thermal model and the findings that will provide inputs to our water segregation model.

The size of the known bodies in the solar system has a large range, but the particular sizes we wish to focus on are the smaller bodies (< 500 km radius). These bodies are the best for us to concentrate on for several reasons. These bodies are abundant, in both the Asteroid Belt and Kuiper Belt. At this size, most of the heat from accretion will be lost to space; therefore the initial planetesimal is “cold”. Finally,

internal pressure will be small enough that we will not need to consider solid-state phase changes in ice, or pressure effects on various parameters.

We assume that the only heat source that affects the system is from radioactive decay. In the early solar system radiogenic heating was especially strong because of the short lived radiogenic elements that existed. The key elements that are hypothesized to contribute to this heat are ^{60}Fe , ^{40}K , ^{232}Th , ^{238}U , ^{235}U , and ^{26}Al . The last element, ^{26}Al , initially produces orders of magnitude more heat than the other isotopes, but decays very quickly (half-life = 700,000 years). Therefore the amount of heat produced is uncertain because the abundance of ^{26}Al will change strongly with small changes in the time of accretion.

If we assume a chondritic abundance of radiogenic isotopes, most bodies below 150 km radius that are in thermal equilibrium will never reach the melting temperature of water ice, unless there is another heat source (Farrell et al., 2007). In larger bodies, radiogenic heating will raise the internal temperature to the melting point. Extremely cold exterior temperatures may maintain a frozen crust of ice and rock. The thickness of this frozen shell will depend on the rate of heating and size of the body. For the purposes of this thesis, we will consider only this “melting core” of the planetesimal (**Fig. 1**), and assume that an overlying shell remains frozen. The radius of the melting core will be denoted by R_0 , and contains the compacting rock/ice/water mixture as well as any meltwater that segregates to the surface of the core. We will later explore a range of sizes of the melting core, recognizing that this radius of the planetesimal is somewhat larger.

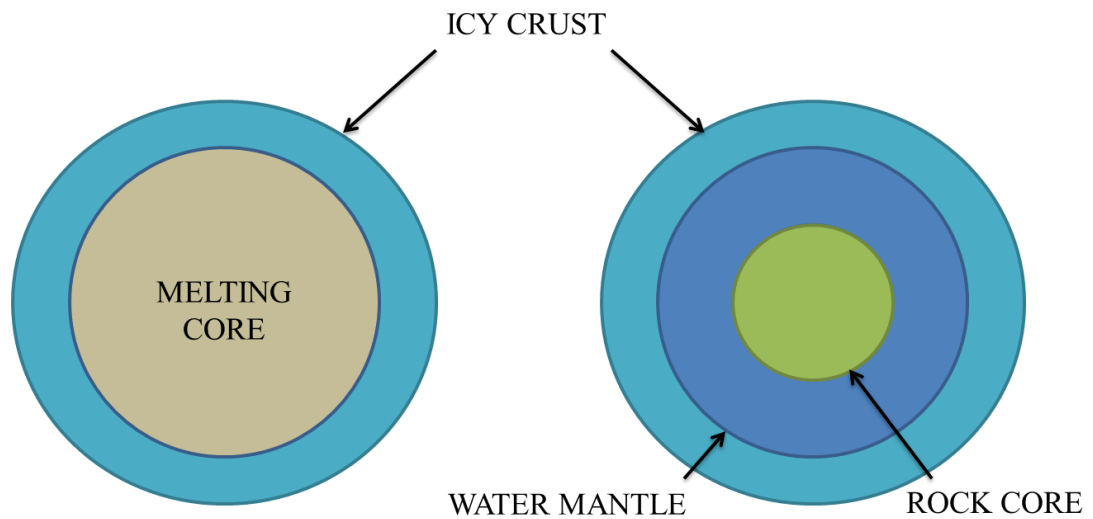


Figure 1: The system as it appears at the beginning of melting and after the completion of segregation.

Further heating goes into the latent heat of the phase change of the ice, buffering temperatures at the melting point. Temperatures throughout the core do not begin to increase again, until all the interior ice is melted completely. This process has been predicted to take between 1 and 150 million years for planetesimals less than 500 km in radius, depending on size, initial concentration of ^{26}Al , and the role of serpentinization (Farrell et al., 2007). Serpentinization, an exothermic reaction caused by liquid water reacting with olivine, is a significant heat source inside of small planetesimals. This reaction is also a large source of hydrogen for the system, which is significant because if this element is able to make it to the liquid layer it is a potential energy source for the evolution of organisms.

2.2 Compaction and Fluid Migration

The initial planetesimal we envision is a mixture of solid ice and rock. When the ice in the core melts, a fluid phase segregates to the top of the core to form a liquid mantle. The segregation process is driven by buoyancy due to the differing densities of the solid and liquid materials. These densities will depend on composition; liquid water is denser than the solid ice, but less dense than rock. Since we are only considering planetesimals with some significant fraction of rock, the solid rock/ice mixture will always be denser than the liquid water. Segregation of the phases requires two other characteristics of the system: there must be a permeable network that allows fluid flow; and the solid phase must be able to deform and compact, in order to fill space vacated by the fluid.

As the temperature of the planetesimal initially increases, the ice produces melt in pockets and creates pore spaces around the edges of the ice crystals. When the melt fraction reaches some critical amount, the pore spaces connect with each other to form a permeable network. This critical amount is determined by the dihedral angle in a water/ice system. This is the angle between two water-ice surfaces at the triple junction of two ice grains and a water-filled pore that is in textural equilibrium, and is determined by the surface energies in the system. If the dihedral angle is $> 60^\circ$, then the equilibrium distribution of water will be isolated pores. The low dihedral angles, $< 30^\circ$, measured in water/ice systems (Mader, 1992) imply that these permeable networks can form at very low melt fractions ($< 1\%$). The resulting fluid networks will extend to all portions of the planetary body that are above the solidus temperature. Where the temperature is below the solidus, water in small pores quickly freezes. Because surface temperatures in the

outer solar system are very low (< 100 K), there will typically be a sub-solidus surface crust. Therefore water will migrate upward and collect in a liquid layer beneath the frozen crust (as in Europa and other icy satellites).

Because the ice is deformable at temperatures near its solidus, we can treat the “solid” matrix of ice and rock as a very viscous fluid. As the solid deforms it allows the liquid to move through the networks that have developed. This makes the problem analogous to the mantle melting/magma migration problem; this problem has been studied by several workers (Asimow 2002, Richter & McKenzie 1984, McKenzie 1984, Ribe 1985b, Rabinowicz & Toplis 2009, Scott and Stevenson, 1986, & Sparks and Parmentier, 1991). The problem of magma segregation differs from typical approaches to porous flow in geologic systems in that the “porosity” here is not a fixed characteristic of the rock, but a varying quantity that depends on the dynamics of the system. As demonstrated by McKenzie, 1984, and Spiegelman, 1993b, it is necessary to account for the viscous deformation of the “solid” phase, since it can offer significant resisting force, and therefore control the timing of melt segregation.

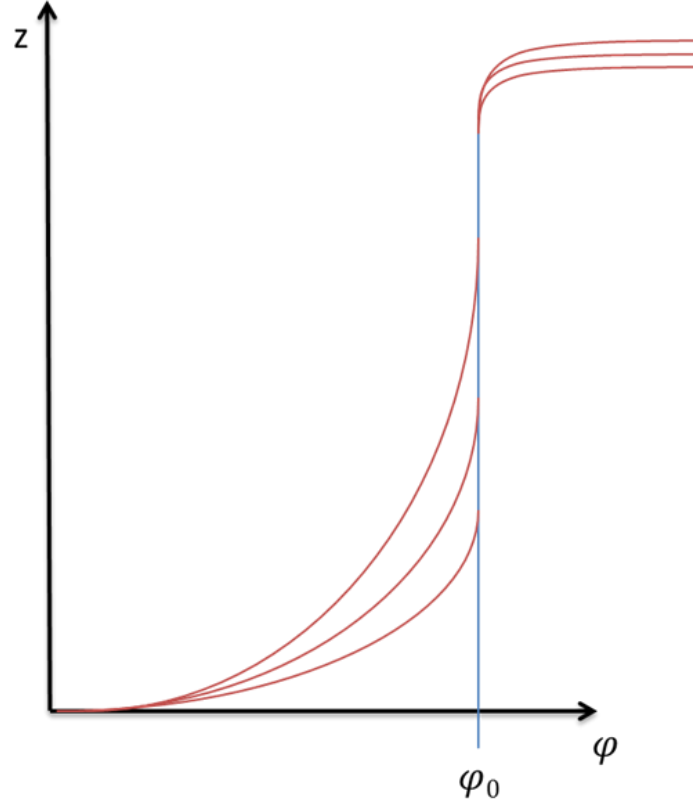


Figure 2: Schematic diagram of the evolution of porosity vs. height in a 1-D column with an initially small and uniform porosity (blue line). This is based on the problem solved in Richter & McKenzie (1984), and solved in Section 5.

The schematic **Fig. 2** shows the evolution of the porosity (φ)-depth (z) relationship of a simplified one-dimensional compacting system that starts with an initially uniform porosity, φ_0 . The vertical axis is height above an impermeable base, below which compaction cannot occur (in our problem, this is the center of the planetesimal). The red lines show porosity at different times. Porosity decreases in a region near $z = 0$, the compacting layer. Above this, where porosity is uniform, water is flowing upward and the solid phase downward, but the solid is not compacting. At the

top of the layer, porosity increases to 1 where the fluid layer collects. The equations that describe the two-phase system break down in this region, so it will not be part of our calculation.

Melt buoyancy is the driving force for segregation. It is opposed by the interphase frictional resistance (the permeability of the matrix) and by the resistance of the solid phase to deformation and compaction. Which of these two resisting forces is dominant depends on the properties of the material. McKenzie (1984) defined a characteristic length scale over which compaction resistance is important. The “compaction length”,

$$\delta_c = \left[\frac{[\zeta + 4/3 \eta]}{\mu} K \right]^{1/2} \quad \text{Eq. 1}$$

depends on the shear (η) and bulk viscosity (ζ) of the solid, the viscosity of the fluid (μ) and the permeability (K) of the matrix. The permeability is assumed to follow a Kozeny-Karman type of law, which depends on the grain size and nonlinearly on the porosity. If compaction occurs over a distance that is small compared to δ_c then compaction stresses are dominant in determining the segregation rate. If compaction is spread over a large area compared to δ_c , then compaction stresses are negligible.

The temporal evolution of a given planetesimal will depend on the size of the partially molten part of the planetary body, compared to the compaction length scale. If the system is many compaction lengths in height, then the solid resistance force will be mostly negligible and segregation will be faster. It is important to realize, however, that even if the compaction forces are small in most of the system, they must be included in

order to impose a no-motion boundary condition at the bottom (center of the planetesimal). Therefore the full problem, including compaction forces, must be solved. If the system is only a few compaction lengths in size, then the compaction stresses will largely control how fast segregation can occur.

To estimate the range of relevant compaction lengths for icy planetesimals we first estimate the permeability of the system. Using a Kozeny-Carman type of relation (McKenzie 1984), a porosity of 0.03 and grain sizes from .0001 - .01 m, permeabilities will range from $\sim 10^{-16}$ to 10^{-12} m². The viscosity of water is 10^{-3} Pa s. Finally the combination of bulk and shear viscosities of the solid phase will result from the two solid phases. We represent this viscosity as a single variable, η_m , the viscosity of the ice/rock mixture.

The viscosity of ice near 0 C to be 10^{14} Pa·s, (McCord & Sotin, 2005) However, mixture viscosity of the “solid” phase in this problem depends on the ratio of the viscously deformable phase (ice) to the rigid solid phase (rock). To determine the value of the viscosity we use a model that was experimentally determined for the effective viscosity of a fluid that contains a high concentration of rigid grains (Nian-Sheng and Wing-Keung, 2003).

$$\eta_m = \eta_i * \exp \left[\frac{2.5}{\beta} \left(\frac{1}{(1 - X_{Rock})^\beta} - 1 \right) \right] \quad \text{Eq. 2}$$

X_{Rock} is the volume fraction of rigid grains in the mixture, η_i is the viscosity of pure ice, and β is an experimental parameter determined to be between 1.6 and 2.5 for the type of

system we are constructing. **Figure 2** shows how the mixture viscosity varies with the rock fraction.

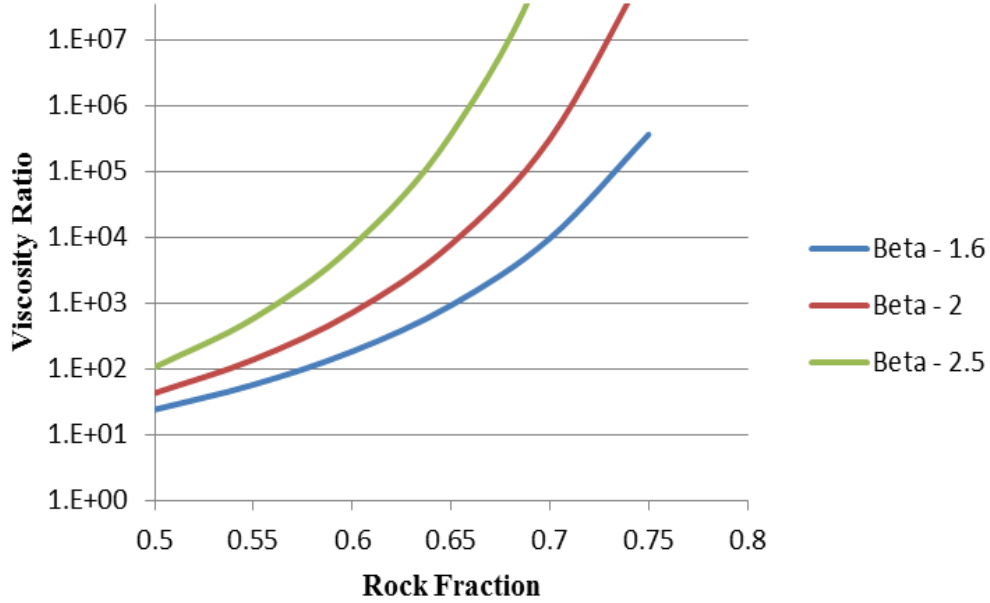


Figure 3: Mixture Viscosity from **Eq. (2)** scaled by the viscosity of the pure system as a function of rock fraction, for three choices of the empirical parameter β .

Figure 3 shows that the initial viscosity of the solid phase in a planetesimal that is 50% rock by volume is 30 – 100 times the value of ice. However, by the time melting and segregation have concentrated the rock phase in the core to 70 %, the viscosity has increased by a further 2.5-5 orders of magnitude. At very high rock fractions, the mixture viscosity from **Eq. (2)** becomes infinite. In the results presented in this thesis, we found it practical to use only a single value of solid viscosity for an entire model run. A result of this simplification is that we allow the core to compact to nearly 100% rock,

squeezing out all water. We explore values of η_m ranging over several orders of magnitude.

The effective compaction length of the problem, the distance over which compaction stresses are important, depends on this mixture viscosity:

$$\delta_c = \left[\frac{\eta_m}{\mu} K \right]^{1/2} \quad \text{Eq. 3}$$

Figure 3 shows the variation of compaction length with the rock fraction of the solid. Compaction length varies from a few hundred meters to thousands of km. Therefore, in a planetesimal with radii in the range of a few hundred km, compaction stresses could be either completely negligible or extremely important throughout the compacting system, depending on the assumed mixture viscosity, as seen in **Figure 4**.

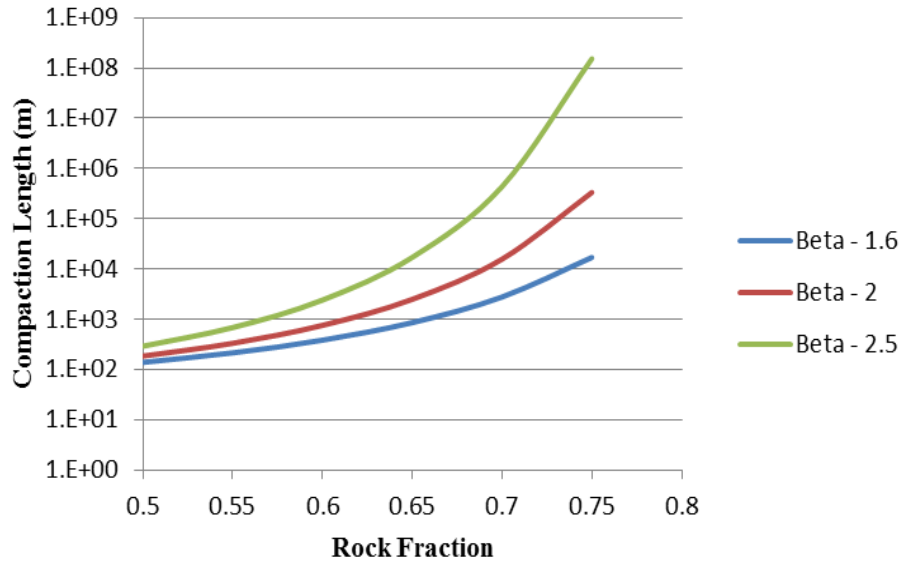


Figure 4: Compaction length vs. rock fraction from **Eq. (3)**, where the solid viscosity is given by **Eq. (2)** with three different values of the parameter β . The permeability is taken to be 10^{-15} m^2 , and the fluid viscosity is $10^{-3} \text{ Pa}\cdot\text{s}$.

As previously described our model is best suited to study planetesimals with melting cores with radii between 50 and 500 km. Since the problem is scaled by the compaction length, we only need determine a range of scaled radii of a melting core ($h = \frac{R_0}{\delta_c}$). However, because there is a large range of permissible estimates of the viscosity of the solid phase, the compaction length is not that well determined. With a range of mixture viscosity estimates between 10^3 and 10^6 times the viscosity of ice, the desired range of core radii are modeled by h values ranging from 10 to 1000. A particular value of h will correspond to a range of core sizes, depending on what estimate of mixture viscosity is assumed. **Fig. 5** shows the h values for any given combination of mixture viscosity and core size. Since the required resolution in the numerical solution is several grid points per compaction length (we use ten), the large h values are expensive to calculate. However, for very large values of h , the compaction stresses are negligible in almost the entire column, so the solutions in this range are easily predictable. Therefore we restrict our later simulations to h values from 5 to 75. A simulation with a particular value of h will correspond to a planetesimal of a range of sizes, depending on what estimate of mixture viscosity is assumed. One point to keep in mind is that the radius we are analyzing is that of the melting core not the whole planetesimal. However, in all but the coolest planetesimals, a large fraction of it will undergo melting.

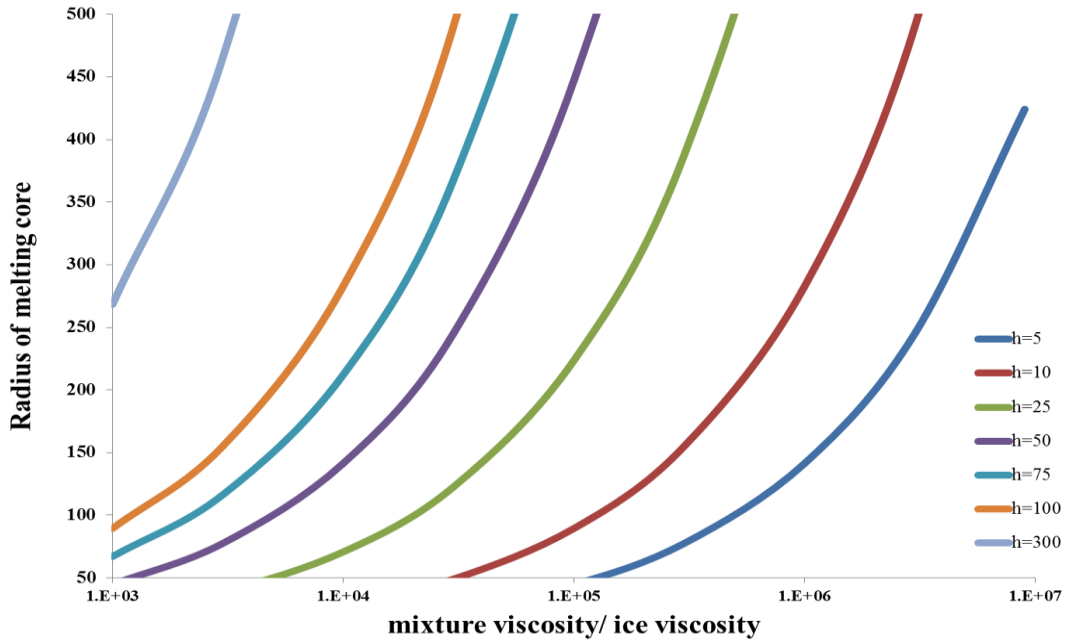


Figure 5: A contour map of h values (core radius/compaction length) as a function of core radius and viscosity ratio. The compaction length assumes a core permeability of $8 \times 10^{-15} \text{ m}^2$.

Due to the nonlinear dependence of permeability on porosity, any spatial variability in porosity will result in strongly correlated variations in melt velocity that cause the porosity variations to grow. In the absence of any compaction stresses (the resistance of the solid phase to deform quickly), perturbations can grow into “shock waves” of porosity: Because the “speed” of porosity migration is strongly dependent on the porosity, perturbations migrate upward and the leading edge will sharpen into a discontinuity in porosity (Spiegelman, 1993a).

Compaction stresses allow porosity variations to grow, but add a length scale (the compaction length) over which these variations must occur. Instead of porosity discontinuities, “waves” of porosity with finite wavelength will form. Waves of high

porosity migrate through the material at a velocity faster than that of the melt itself, and each wave will tend to create a chain behind it as it moves. There is a rich set of dynamics that arise from this effect, described as “solitary waves” (Spiegelman, 1993a) or “magmons” (Scott and Stevenson, 1986).

Any disturbance, such as a boundary layer, will tend to lead to the formation of chains of melt waves that propagate upwind (opposite the melt flow direction) from the disturbance. The tracking of these waves is beyond the scope of this work since the total time to extract melt from a region is not greatly affected by the waves. We carefully choose our boundary conditions to minimize this effect, but porosity waves are clearly visible in many of our numerical results.

2.3 Melting and Compaction in a Planetsimal Core

There are several significant differences between the mantle magma migration problem, and the problem that we will address, that of a compacting spherical core. The first is the obvious one of geometry, which will slightly change the equations (see section 3). In addition, the gravitational driving force in this situation is significantly different, in that it varies in time and space. Finally, the melting term provides a source of fluid that, combined with compaction stresses, controls how the distribution of rock, ice, and water evolve.

The driving force behind the segregation of the phases depends on the magnitude of the gravitational acceleration, and also on the density difference between the phases.

In the spherical melting core, gravity will increase outward from the center of the core,

$$g(r) = \frac{4\pi\sigma \int_0^r \rho(r)r^2 dr}{r^2}$$

If the fluid fraction remains small, we can assume the density is approximately given by the solid density, which is nearly uniform in the core.

$$g(r) = \frac{4\pi}{3} G \rho_s r \quad \text{Eq. 4}$$

So the gravity force, far from being uniform, varies linearly with radius and vanishes at the center of the core. This effect slows migration near the center of the core.

A further variation in the driving term comes from the density difference between solid and melt which increases as the core becomes more rock-rich during segregation.

$$\Delta\rho = (\rho_s - \rho_w) \quad \text{Eq. 5}$$

$$\rho_s = \frac{(\rho_I X_{Ice} + \rho_R X_{Rock})}{(X_{Ice} + X_{Rock})} \quad \text{Eq. 6}$$

where X represents the volume fraction of the different phases.

The production of meltwater is determined by the rate of radioactive decay. Following McCord and Sotin (2005), we calculate the heat production from a particular concentration of radioactive isotopes at some initial time $t = 0$, which represents the time of the beginning of solid accretion in the solar system. The concentration of isotope, i , in parts per billion (*ppb*) follows:

$$C^i = C_0^i \cdot e^{\left(\frac{t}{t_h^i}\right)}$$

where C_0^i is the concentration at $t = 0$ and t_h^i is the half-life. The heat given off by the isotopes' decay, Q_i , per kg of rock is

$$Q^i = H^i C^i$$

where H^i is the rate of heat production per kg of isotope. These values are given in Table 1.

Isotope	Half-Life (yr.), t_h^i	Initial Concentration (ppb), C_0^i	Heat Produced Rate (mW/kg), H^i	Total Heat (mW/kg rock), Q^i
Uranium – 235	7.04×10^8	17.5	4.01×10^{-4}	7.0175×10^{-12}
Uranium – 238	4.47×10^9	52.4	1.04×10^{-4}	5.4496×10^{-12}
Potassium – 40	1.28×10^9	430	6.19×10^{-5}	2.6617×10^{-11}
Thorium – 232	1.41×10^{10}	130	2.04×10^{-5}	2.65×10^{-12}
Aluminum – 26	7.17×10^5	450	.138	6.21×10^{-8}
Iron - 60	2.6×10^6	.8	.0747	5.976×10^{-11}

Table 1: These are the values of each element for the concentration, heat produced, and the combined value at a time of zero million years before accretion. (McCord & Sotan, 2005)

The total radiogenic heating is given by the sum of the Q values.

$$Q = \sum_i Q^i$$

We will approximate the concentration of radiogenic isotopes in the ice and water phases as 0. Therefore, the total heat production rate will be Q times the volume fraction of rock.

The melting rate, Γ , is defined as the rate of mass exchange from solid ice to water per unit volume $\left(\frac{kg}{m^3 \cdot s}\right)$. For a core that is at the melting temperature of ice, all of the heat production goes into latent heat. The rate of melting ice is therefore

$$\Gamma = \frac{QX_{rock}\rho_{rock}}{L} \quad \text{Eq. 7}$$

where L is the latent heat of ice. For a fixed value of $X_{rock} = 0.5$, the melting rate is plotted as a function of accretion time in Figure 5. At this rock fraction, the initial core contains 500 kg of ice per m^3 . Therefore total melting time at a given fixed value of Γ is given by

$$t_{melt} = \frac{500}{\Gamma}$$

for $\Gamma = 10^{-11} \frac{kg}{m^3 \cdot s}$ the time required to melt all the ice present is only 1.6 M.y.

Since the total melting times are relatively short, the decay of melting rate with time is not very large (on the order of a factor of 2-4). During this time, compaction and expulsion of the ice phase will increase the concentration of rock and the heating in the core by up to a factor of 2 somewhere counteracting this decay. The dominant heat source, ^{26}Al , decays so quickly, a variation of a few million years in the time of accretion of different planetesimals will lead to a large variation in heating rates, even if they have the same isotopic composition. Therefore, for simplicity, we hold melting rate constant during a simulation, and simply choose widely different initial melting rates that approximate different accretion times.

In the simulations we will present in section 5, we explored two different rates of melting which represent reasonable values that could be produced by radiogenic heating. These two rates, 4.46×10^{-11} and 6.27×10^{-13} , correspond to accretion times of 860,000 years and 6.71 million years. For a melting core that is 50% ice, and assuming no migration of the water, these two melting rates would completely melt the ice component in 0.36 and 25 My, respectively. Figure 6 is the representation of the melting rate as it evolves through the time of accretion.

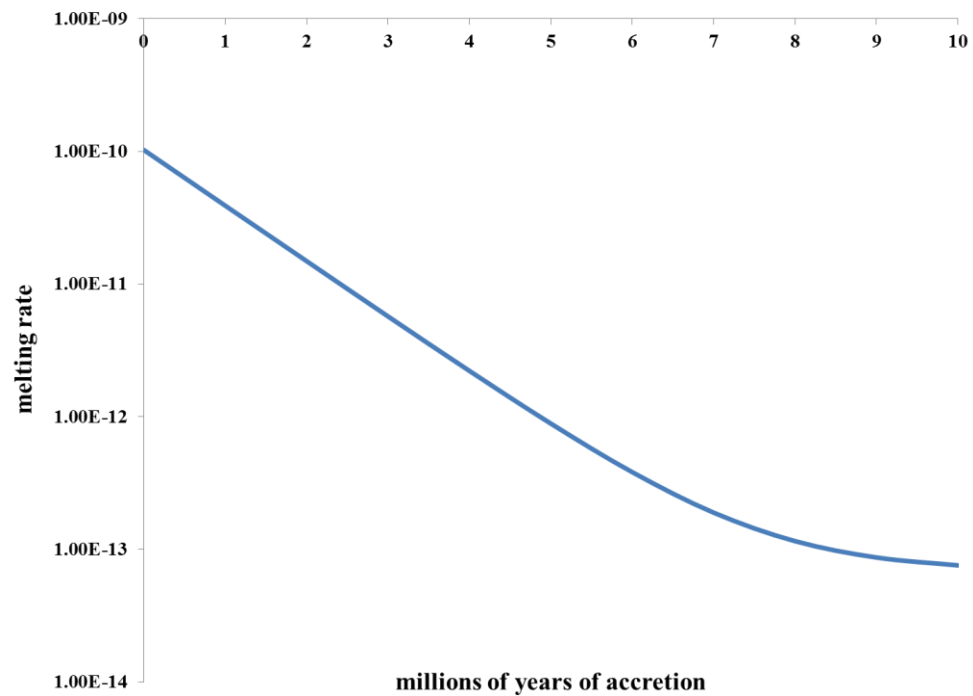


Figure 6: Melting rate vs. the time of accretion for a planetesimal. The consultants which we have used in the previously described equations were taken from Table 1.

<u>Variable</u>	<u>Meaning</u>	<u>Values</u>	<u>Dimensions</u>
\mathbf{z}	Unit vector in Vertical direction		\mathbf{m}
\mathbf{r}	Unit vector in Radial direction		\mathbf{m}
θ	Unit vector in Latitudinal direction		$Deg.$
Ψ	Unit vector in Longitudinal direction		$Deg.$
t	Time		s
W	Solid Velocity		$\mathbf{m} \cdot \mathbf{s}^{-2}$
ω	Liquid Velocity		$\mathbf{m} \cdot \mathbf{s}^{-2}$
g	Acceleration due to Gravity		$\mathbf{m} \cdot \mathbf{s}^{-2}$
ρ_f	Density of Melt	1×10^3	$\mathbf{kg} \cdot \mathbf{m}^{-3}$
ρ_I	Density of Ice	1×10^3	$\mathbf{kg} \cdot \mathbf{m}^{-3}$
ρ_R	Density of Rock	3×10^3	$\mathbf{kg} \cdot \mathbf{m}^{-3}$
ρ_s	Density of Matrix	2×10^3	$\mathbf{kg} \cdot \mathbf{m}^{-3}$
$\Delta\rho$	Density Difference ($\rho_s - \rho_f$)	$1 \times 10^3 - 2 \times 10^3$	$\mathbf{kg} \cdot \mathbf{m}^{-3}$
X_{Ice}	Concentration of Ice	$0 - 0.5$	
X_{Rock}	Concentration of Rock	$0.5 - 1.0$	
φ	Porosity of Matrix		
Γ	Melting Rate	$4.46 \times 10^{-11} - 6.23 \times 10^{-13}$	$\mathbf{kg} \cdot \mathbf{t}^{-1} \cdot \mathbf{m}^{-3}$
P	Fluid Pressure		\mathbf{Pa}
μ	Dynamic Shear Viscosity of Melt	10^{-3}	$\mathbf{Pa} \cdot \mathbf{s}$
K	Specific Permeability		\mathbf{m}^2
D	Fluid-Solid Drag Resistance		$\mathbf{kg} \cdot \mathbf{s}^{-1}$
δ_c	Compaction Length		\mathbf{m}
ζ	Bulk viscosity of matrix		$\mathbf{Pa} \cdot \mathbf{s}$
ζ^*	$=(1 - \varphi)\zeta$	$10^{17} - 10^{21}$	$\mathbf{Pa} \cdot \mathbf{s}$
η	Shear viscosity of matrix		$\mathbf{Pa} \cdot \mathbf{s}$
η^*	$=(1 - \varphi)\eta$	$10^{17} - 10^{21}$	$\mathbf{Pa} \cdot \mathbf{s}$
q	Mass Flux		$\mathbf{m}^3 \cdot \mathbf{m}^{-2} \cdot \mathbf{s}^{-1}$
τ	Designed Constant		\mathbf{m}
η_m	Mixture Viscosity		$\mathbf{Pa} \cdot \mathbf{s}$
β	Exponent in Viscosity Equations	$1.0 - 2.4$	
G	Gravitation Constant	$\frac{2}{3} \times 10^{-10}$	$\mathbf{m}^3 \cdot \mathbf{kg}^{-1} \cdot \mathbf{s}^{-2}$
γ	$\left(\zeta + \frac{2}{3}\eta\right) / \left(\zeta + \frac{4}{3}\eta\right)$	$\frac{5}{7}$	

Table 2: This table is a listing of variables that we use in the thesis, including the meanings of each variable range of assigned values and the respective units for each.

3. THE GOVERNING EQUATIONS OF COMPACTION

3.1 Compaction Equations in Cartesian Coordinates

The equations that govern the melt migration process were derived originally by McKenzie (1984). The vector form conservation of mass for each of the three phases (melt, rock, and ice) are written

$$\frac{\partial(\rho_f \varphi)}{\partial t} + \nabla \cdot [\rho_f \varphi \vec{\omega}] = \Gamma \quad \text{Eq. 8}$$

$$\frac{\partial(\rho_R(1 - \varphi))}{\partial t} + \nabla \cdot [\rho_R(1 - \varphi) \vec{W}] = 0 \quad \text{Eq. 9}$$

$$\frac{\partial(\rho_I(1 - \varphi))}{\partial t} + \nabla \cdot [\rho_I(1 - \varphi) \vec{W}] = -\Gamma \quad \text{Eq. 10}$$

In these equations we have variables assigned to the rate of melting (Γ) (the mass transfer from the ice phase to the liquid phase), melt (ρ_f), rock (ρ_R), and solid ice (ρ_I) densities (taken to be constant here), melt ($\vec{\omega}$) and solid (\vec{W}) velocities, and the porosity (φ) of the matrix. Here we assume that the two mixed solid phases have the same velocity, but only the ice undergoes the phase change. Note that porosity here does not denote a fixed property of rock, but the fraction of melt in a given volume, which therefore varies in space and time. We can combine the ice and rock equations to get a single conservation equation for the solid:

$$\rho_I \frac{\partial((1 - \varphi))}{\partial t} + \rho_I \nabla \cdot [(1 - \varphi) \vec{W}] = -\Gamma \quad \text{Eq. 11}$$

Because we will assume that the two solid phases do not move relative to each other, we will also treat them as a single phase in the momentum equation. The conservation of momentum in fluid and solid phase is given by;

$$-\rho_f \varphi g \vec{z} - \vec{D} + \nabla \cdot [\varphi \bar{\bar{\sigma}}^f] = 0 \quad \text{Eq. 12}$$

$$-\rho_s(1 - \varphi)g\vec{z} + \vec{D} + \nabla \cdot [(1 - \varphi)\bar{\bar{\sigma}}^s] = 0 \quad \text{Eq. 13}$$

Note that in **Eq. (13)** we use the solid matrix density ρ_s as opposed to the conservation of mass problems, where we have used the density of ice ρ_I . The density of the solid matrix ρ_s is given by **Eq. (6)**.

The slow melting and deformation in this problem means that we can neglect acceleration terms, i.e. this is a low Reynolds number system. Therefore buoyancy forces are balanced by an interphase drag exerted between the solid and liquid phases, \vec{D} , and by gradients in stress. The melt has a relatively low viscosity and it is assumed that viscous resistance to fluid deformation is small relative to pressure gradients and will be subsumed into the fluid-solid drag resistance term. Therefore the melt stress tensor is given by the pressure, P :

$$\bar{\bar{\sigma}}^f = -P\bar{\bar{I}}$$

where $\bar{\bar{I}}$ is the identity tensor. The stress tensor for the solid phase includes viscous resistance to both shear and compaction (volume change).

$$\bar{\bar{\sigma}}^s = -P\bar{\bar{I}} + \zeta\Delta\bar{\bar{I}} + 2\eta(\bar{\bar{\epsilon}}^s - \frac{\Delta}{3}\bar{\bar{I}})$$

Here ζ is the bulk viscosity and η is the shear viscosity of the solid, $\bar{\bar{\epsilon}}^s$ is the strain rate tensor of the solid, and Δ is defined as the *compaction rate* of the solid:

$$\Delta \equiv \nabla \cdot \vec{W}$$

To follow what was done by McKenzie (1984) the interaction force exerted by the solid and fluid phases on each other is given as

$$\vec{D} = \frac{\mu\varphi^2}{K}(\vec{\omega} - \vec{W}) - P\nabla\varphi \quad \text{Eq. 14}$$

where μ and K , are the dynamic shear viscosity of the melt and the permeability of the matrix respectively. This form of interaction force ensures that, in the absence of compaction forces, the problem reduces to Darcy's Law for flow through a permeable matrix.

$$(\vec{\omega} - \vec{W}) = -\frac{K}{\mu\varphi}(\nabla P + \rho_f g \vec{z}) \quad \text{Eq. 15}$$

In these equations we also assume the permeability is a nonlinear function of porosity (Richter & McKenzie, 1984):

$$K = \frac{a^2\varphi^n}{b}$$

where a is grain size of the solid phase, b is a scaling constant (1000), and the exponent n is 3. Finally, we will make the assumption that spatial variation in both the solid fraction $(1 - \varphi)$ and solid viscosities are small compared to variation in solid velocity. Following McKenzie, for compactness, we redefine viscosities to simplify the calculations:

$$\zeta^* = (1 - \varphi)\zeta$$

$$\eta^* = (1 - \varphi)\eta$$

Substitute **Eq. 14** into both **Eqs. 12 & 13** and gives;

$$-\rho_f \phi g \vec{z} - \frac{\mu \phi^2}{K} (\vec{\omega} - \vec{W}) - \phi \nabla P = 0 \quad \text{Eq. 16}$$

$$\begin{aligned} -\rho_s(1 - \phi)g \vec{z} + \frac{\mu \phi^2}{K} (\vec{\omega} - \vec{W}) - (1 - \phi)\nabla P + \left(\zeta^* + \frac{\eta^*}{3}\right) \nabla(\nabla \cdot \vec{W}) + \eta^* \nabla^2 \vec{W} \\ = 0 \end{aligned} \quad \text{Eq. 17}$$

We subtract **Eq. (16)** from **Eq. (17)** and then substitute **Eq. (15)** to obtain an equation in velocities that eliminates pressure:

$$-\Delta \rho(1 - \phi)g \vec{z} + \frac{\mu \phi}{K} (\vec{\omega} - \vec{W}) + \left(\zeta^* + \frac{\eta^*}{3}\right) \nabla(\nabla \cdot \vec{W}) + \eta^* \nabla^2 \vec{W} = 0 \quad \text{Eq. 18}$$

Richter and McKenzie (1984) have described a simpler one-dimensional problem, in which porosity and velocity vary only in the vertical direction. In this system the conservation of mass (**Eq. 8 & 11**) are given by

$$\frac{\partial \phi}{\partial t} + \frac{\partial(\phi \omega)}{\partial z} = \frac{1}{\rho_f} \Gamma \quad \text{Eq. 19}$$

$$\frac{\partial(1 - \phi)}{\partial t} + \frac{\partial}{\partial z} [(1 - \phi)W] = -\frac{1}{\rho_s} \Gamma \quad \text{Eq. 20}$$

and the conservation of momentum is

$$-\rho_f \phi g - \frac{\mu \phi^2}{K} (\omega - W) + \phi \frac{\partial P}{\partial z} = 0 \quad \text{Eq. 21}$$

$$-\rho_s(1 - \phi)g + \frac{\mu \phi^2}{K} (\omega - W) - (1 - \phi) \frac{\partial P}{\partial z} + \left(\zeta^* + \frac{4}{3} \eta^*\right) \frac{\partial^2 W}{\partial z^2} = 0 \quad \text{Eq. 22}$$

These two momentum equations (**Eq. 21 & 22**) are combined with Darcy's Law (**Eq. 15**) to again eliminate the pressure,

$$\left(\zeta^* + \frac{4}{3} \eta^*\right) \frac{\partial^2 W}{\partial z^2} - (\rho_s - \rho_f)(1 - \phi)g + \frac{\mu \phi}{K} (\omega - W) = 0 \quad \text{Eq. 23}$$

The two mass equations (**Eq. 19** and **20**) are combined and integrated to solve for the fluid velocity in terms of the solid velocity and melting rate:

$$\omega = -\frac{(1-\varphi)W}{\varphi} + \frac{1}{\varphi} \int \left(\frac{1}{\rho_f} - \frac{1}{\rho_s} \right) \Gamma dz \quad \text{Eq. 24}$$

Substituting **Eq. 22** into the combined momentum equation (**Eq. 21**) gives an equation for the solid velocity:

$$\left(\zeta^* + \frac{4}{3} \eta^* \right) \frac{\partial^2 W}{\partial z^2} - \Delta \rho (1 - \varphi) g - \frac{\mu}{K} \left(-W + \int \left(\frac{1}{\rho_f} - \frac{1}{\rho_s} \right) \Gamma dz \right) = 0 \quad \text{Eq. 25}$$

Eqs. 20 & 25 are the final pair of differential equations that can be solved for W and φ to determine the evolution of fluid segregation.

We also need to specify boundary and initial conditions. Richter & McKenzie model a non-melting permeable system that is compacting onto a rigid impermeable surface at $z = 0$. Therefore, the bottom boundary condition is:

$$W(0) = 0 \quad \text{Eq. 26}$$

At the top of the compacting layer a pure liquid layer develops, within which the equations of a permeable medium break down. Richter and McKenzie claim to apply the boundary conditions of no compaction

$$\left. \frac{dW}{dz} \right|_{z=z_d} = 0$$

and fixed porosity

$$\varphi_t^{z=z_d} = \varphi_0$$

at the top of this partially molten mixture, $z = z_d$. The position z_d drops in time, as the system compacts at a rate determined by the solid velocity;

$$\frac{d(zd)}{dt} = W(z = z_d)$$

These boundary conditions are reasonable during early stages of compaction, when porosity changes only near the bottom boundary, and most of the column is simply passing fluid to the surface, following Darcy's Law. However, the figures shown in Richter and McKenzie clearly show that at later times, as z drops, porosity does not remain constant and velocity gradients do not remain zero. It is unclear what conditions were actually applied in this study since their figures also truncate the uppermost part of the curve where porosity waves should begin to develop. We wish to use a boundary condition that will allow an unimpeded flow of melt out of the top of the partially molten region and into the fluid layer, generating as little porosity disturbance as possible that can propagate downward as waves. After several trials, we found that setting the gradient in the flux of solid to zero at this boundary is the most effective condition.

$$\left. \frac{d(1 - \varphi)W}{dz} \right|_{z = z_d} = 0 \quad \text{Eq. 27}$$

3.2 Compaction Equations in Spherical Core

In a spherical coordinate system, with r , θ , and Ψ representing the radial, latitudinal, and longitudinal directions, the divergence of a vector $\vec{F} = a\vec{e}_r + b\vec{e}_\theta + c\vec{e}_\Psi$ is written as:

$$\nabla \cdot \vec{F} = \frac{1}{r^2} \frac{\partial}{\partial r} (ar^2) + \frac{1}{r \sin \theta} \frac{\partial}{\partial \theta} (b \sin \theta) + \frac{1}{r \sin \theta} \frac{\partial c}{\partial \Psi}$$

For a radially symmetric problem, the last two terms will be zero;

$$\nabla \cdot \vec{F} = \frac{1}{r^2} \frac{\partial}{\partial r} (ar^2)$$

Applying the product rule gives:

$$\nabla \cdot \vec{F} = \frac{\partial a}{\partial r} + \frac{2a}{r}$$

where the second term comes about from the radial spreading with increasing r .

This makes the radial conservation of mass and momentum equations:

$$\frac{\partial \varphi}{\partial t} + \frac{\partial [\omega \varphi]}{\partial r} + \frac{2\omega \varphi}{r} = -\frac{1}{\rho_f} \Gamma \quad \text{Eq. 28}$$

$$\frac{\partial (1 - \varphi)}{\partial t} + \frac{\partial [(1 - \varphi)W]}{\partial r} + \frac{2(1 - \varphi)W}{r} = -\frac{1}{\rho_l} \Gamma \quad \text{Eq. 29}$$

$$-\rho_f \varphi g - \frac{\mu \varphi^2}{K} (\omega - W) + \varphi \frac{\partial P}{\partial r} = 0 \quad \text{Eq. 30}$$

$$\begin{aligned} -\rho_s (1 - \varphi) g - \frac{\mu \varphi^2}{K} (\omega - W) + (1 - \varphi) \frac{\partial P}{\partial r} + \left(\zeta^* + \frac{4}{3} \eta^* \right) \left[\frac{\partial^2 W}{\partial r^2} + \frac{2}{r} \frac{\partial W}{\partial r} \right] \\ + \left(\zeta^* + \frac{2}{3} \eta^* \right) \left[-\frac{2}{r^2} W \right] = 0 \end{aligned} \quad \text{Eq. 31}$$

In the Cartesian analysis, two mass equations are combined to solve for fluid velocity

(See **Eq. 24**). Here, **Eqs. 28 & 29** combine to give

$$\frac{\partial}{\partial r} [\varphi \omega + (1 + \varphi)W] + \frac{2}{r} [\varphi \omega + (1 - \varphi)W] = \left(\frac{1}{\rho_f} - \frac{1}{\rho_l} \right) \Gamma$$

In the limit of large r , the $\frac{1}{r}$ term above is relatively small. At a very small value of r , the velocities go to zero, while velocity gradients are large. In both cases, the $\frac{1}{r}$ term above can be neglected. For convenience then, we assume that (Eq. 22) with z replaced

with r , is approximately valid everywhere in the spherical system as well. Using this and combining the momentum equations to eliminate P gives;

$$\begin{aligned}
-\Delta\rho(1-\varphi)g - \frac{\mu}{K} \left(W - \int \left(\frac{1}{\rho_f} - \frac{1}{\rho_s} \right) \Gamma dr \right) + \left(\zeta^* + \frac{4}{3} \eta^* \right) \left[\frac{\partial^2 W}{\partial r^2} + \frac{2}{r} \frac{\partial W}{\partial r} \right] \\
+ \left(\zeta^* + \frac{2}{3} \eta^* \right) \left[-\frac{2}{r^2} W \right] = 0
\end{aligned} \tag{Eq. 32}$$

Eqs. 29 & 32 are the spherical versions of **Eqs. 20 & 25**, and will be solved using the finite difference method. We make two more simplifications. Since the exact relationship between the shear and bulk viscosity of a viscously-deforming solid is not known, for simplicity we assume they are equal.

$$\zeta^* = \eta^*$$

We will assume that melting rate, Γ , does not vary with radius throughout the core, (i.e., the distribution of radiogenic heat sources remains uniform). Therefore we can substitute:

$$\int \Gamma dr = r\Gamma$$

Making these substitutions, **Eq. (30)** becomes:

$$\begin{aligned}
-\Delta\rho(1-\varphi)g - \frac{\mu}{K} \left(W - \left(\frac{1}{\rho_f} - \frac{1}{\rho_s} \right) r\Gamma \right) + \frac{7}{3} \zeta^* \left[\frac{\partial^2 W}{\partial r^2} + \frac{2}{r} \frac{\partial W}{\partial r} \right] + \frac{5}{3} \zeta^* \left[-\frac{2}{r^2} W \right] \\
= 0
\end{aligned} \tag{Eq. 33}$$

Eq. 33 can be solved for W , and **Eq. 29** is solved for φ , with the same boundary conditions described by **Eq. 26** and **27**.

3.3 Scaling of Spherical Compaction Equations

We scale the system of equations substitution for each variable a dimensionless variable times a scaling constant.

$$t = t_0 t'$$

$$r = \delta_c r'$$

$$W = W_0 W'$$

$$w = W_0 w'$$

$$K = K_0 \varphi'^n$$

$$g = g_0 g'$$

$$\Gamma = \Gamma_0 \Gamma'$$

$$\Delta\rho = \Delta\rho_0 \Delta\rho'$$

$$\eta^* = \frac{7}{3} \eta_0 \eta'$$

$$\varphi = \varphi_0 \varphi'$$

All other quantities (densities of individual phases, fluid viscosities) are treated as constants.

$$\begin{aligned} \frac{1}{t_0} \frac{\partial(1 - \varphi_0 \varphi')}{\partial t'} + \frac{W_0}{\delta_c} \left[\left[\frac{\partial}{\partial r'} (1 - \varphi_0 \varphi') W' \right] + \frac{2(1 - \varphi_0 \varphi') W'}{r'} \right] &= -\frac{\Gamma_0}{\rho_I} \Gamma' \\ -\Delta\rho_0 g_0 (1 - \varphi_0 \varphi') \Delta\rho' g' - \frac{\mu}{K_0 \varphi'^n} \left(W_0 W' - \left(\frac{1}{\rho_f} - \frac{1}{\rho_s} \right) \delta_c \Gamma_0 \Gamma' r' \right) \\ + \frac{7}{3} \frac{W_0 \eta_0}{\delta_c^2} \left[\eta^* \left[\frac{\partial^2 W'}{\partial r'^2} + \frac{2}{r'} \frac{\partial W'}{\partial r'} \right] - \frac{5}{7} \eta^* \left[-\frac{2}{r^2} W \right] \right] &= 0 \end{aligned}$$

We then make dimensionless versions of these equations, by dividing by the scaling constants on the rate of porosity change term, and the compaction stress term, respectively:

$$\begin{aligned} \frac{\partial(1 - \varphi_0 \varphi')}{\partial t'} + \frac{W_0 t_0}{\delta_c} \left[\left[\frac{\partial}{\partial r'} (1 - \varphi_0 \varphi') W' \right] + \frac{2(1 - \varphi_0 \varphi') W'}{r'} \right] &= - \frac{\Gamma_0 t_0}{\rho_l} \Gamma' \\ - \frac{\delta_c^2}{W_0 \eta_0} \Delta \rho_0 g_0 (1 - \varphi_0 \varphi') \Delta \rho' g' - \frac{\mu \delta_c^2}{K_0 \eta_0 \varphi'^n} W' + \frac{\mu \delta_c^3 \Gamma_0}{W_0 \eta_0 K_0 \varphi'^n} \left(\frac{1}{\rho_f} - \frac{1}{\rho_s} \right) \Gamma' r' \\ + \left[\frac{7}{3} \eta^* \left[\frac{\partial^2 W'}{\partial r'^2} + \frac{2}{r'} \frac{\partial W'}{\partial r'} \right] - \frac{5}{7} \eta^* \left[- \frac{2}{r^2} W \right] \right] &= 0 \end{aligned}$$

Following McKenzie (1984), we choose the compaction length as the length scale, the Darcy velocity at a melt fraction of φ_0 as the velocity scale, and the quotient of those two scales as the time scale:

$$\delta_c = \left[\frac{K_0 \left(\zeta^* + \frac{4}{3} \eta^* \right)}{\mu} \right]^{1/2}$$

$$W_0 = \frac{K_0 (1 - \varphi_0) g_0 \Delta \rho_0}{\mu}$$

$$K_0 = \frac{a \varphi_0^n}{b}$$

$$t_0 = \frac{\delta_c}{W_0}$$

For our own problem other scales were needed. The melting rate scale is

$$\Gamma_0 = \frac{\rho_f}{t_0}$$

The maximum gravity at the top of the melting core, $r = R_0$, is taken as the gravity scale,

$$g_0 = \frac{4\pi}{3} G \rho_s R_0$$

and the initial density difference, when the solid phase is 50% rock, is taken as the density difference scale

$$\Delta\rho_0 = (.5(\rho_R + \rho_I) - \rho_w)$$

The porosity scale, φ_0 , can be chosen arbitrarily. We take it to be 0.02, a representative porosity in most of our models. After the substitution we may do away with the primes on dimensionless variables and the non-dimensional equations become:

$$\frac{\partial(1 - \varphi_0\varphi)}{\partial t} + \frac{\partial}{\partial r}(1 - \varphi_0\varphi)W + \frac{2(1 - \varphi_0\varphi)W}{r} = -\frac{\rho_f}{\rho_I}\Gamma \quad \text{Eq. 34}$$

$$-\frac{(1 - \varphi_0\varphi)\Delta\rho g}{1 - \varphi_0} - \frac{W}{\varphi^n} + \left(1 - \frac{\rho_f}{\rho_s}\right)\frac{1}{\varphi^n}\Gamma r + \left[\frac{\partial^2 W}{\partial r^2} + \frac{2}{r}\frac{\partial W}{\partial r}\right] - \gamma\left[-\frac{2}{r^2}W\right] = 0 \quad \text{Eq. 35}$$

where $\gamma = \frac{5}{7}$. The non-dimensional boundary conditions, after dropping primes, are

identical to **Eq. 26** and **27**.

3.4 Numerical Solution

We will solve **Eqs. 31 & 32** numerically by substituting finite differentiation approximations for the derivatives. For the velocity equation we use the centered difference method on all derivatives. The difference equations that holds at grid point i is

$$\begin{aligned} \frac{W_{i+1} - 2W_i + W_{i-1}}{\Delta r^2} - \frac{(1 - \varphi_0\varphi)\Delta\rho_i g_i}{(1 - \varphi_0)\eta} - \frac{W_i}{\eta\varphi_i^n} + \frac{\left(1 - \frac{\rho_f}{\rho_s}\right) \Gamma r_i}{3 \eta\varphi_i^n} + \frac{2}{r_i} \frac{W_{i+1} - W_{i-1}}{\Delta r} \\ + \gamma \left[-\frac{2}{r_i^2} W_i \right] = 0 \end{aligned}$$

The resulting equation for the value of W_i is:

$$W_i = \frac{\left[\frac{(1 - \varphi_0\varphi)\Delta\rho_i g_i}{(1 - \varphi_0)\eta} + \frac{\left(1 - \frac{\rho_f}{\rho_s}\right) \Gamma r_i}{3 \eta\varphi_i^n} - \frac{W_{i+1}}{\Delta r^2} - \frac{W_{i-1}}{\Delta r^2} - \frac{2}{r_i} \frac{W_{i+1} - W_{i-1}}{2\Delta r} \right]}{\left[-\frac{2}{r_i^2} \gamma - \frac{1}{\eta\varphi_i^n} - \frac{2}{\Delta r^2} \right]} \quad \text{Eq. 36}$$

If porosity is completely known at an instant in time, we can solve for the distribution of solid velocity by iterating over **Eq. 36** until convergence.

Since **Eq. 31** is an equation for the solid fraction of the system, we replace the porosity with $\Psi = 1 - \varphi_0\varphi$

$$\frac{\partial \Psi}{\partial t} + \frac{\partial}{\partial r} [\Psi W] + \frac{2\Psi W}{r} = -\frac{\rho_f}{\rho_l} \Gamma$$

We use forward differencing in time and upwind differencing in space:

$$\frac{\Psi_i^* - \Psi_i}{\Delta t} = -\frac{1}{\Delta r} [\Psi_{i+1} W_{i+1}^+ - \Psi_i W_{i-1}^-] - \frac{2\Psi_i W_i}{r_i} - \frac{\rho_f}{\rho_l} \Gamma_i \quad \text{Eq. 37}$$

where Ψ_i^* is the value of Ψ_i after one time step and the values of W_{i+1}^+ & W_{i+1}^- are:

$$W_{i+1}^+ = \frac{1}{2} (W_{i+1} + W_i)$$

$$W_{i+1}^- = \frac{1}{2} (W_i + W_{i-1})$$

At each time step, using the porosity previously determined, we iterate **Eq. 36** using the Gauss-Seidel method, to solve for all of the solid velocities. These solid velocities are then used in **Eq. 37** to solve for a new porosity at the next time step, and the process is then repeated to step through time.

4. SPHERICAL VS. CARTESIAN COMPARISON, NO MELTING

Since the compaction problem has not been solved in a spherical core before, we first present results of a simplified problem to look at the effects of sphericity and variable gravity. In this problem, we will set the melting rate to zero, and just track the segregation of a small amount of melt. This is based on the illustrative 1-D problem done in Richter & McKenzie (1984) with a uniform initial porosity:

$$\varphi(z, t = 0) = \varphi_0$$

Using $\varphi_0 = 0.02$, and the boundary conditions **Eq. 26** and **27**, we redo this problem, both in Cartesian coordinates with a fixed gravity, and in the 1-D radial coordinate system with a radically-varying gravity.

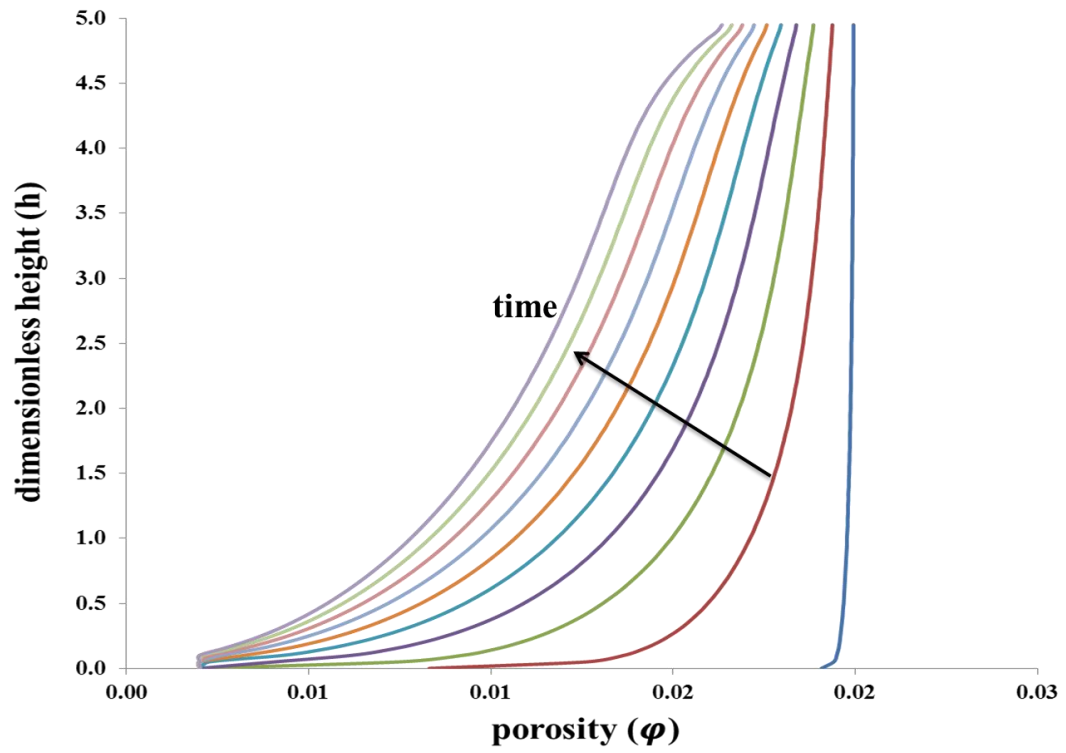


Figure 7: Porosity vs. dimensionless height in a non-melting Cartesian System. The separate curves show porosity at ten uniformly spaced times after the initiation of compaction.

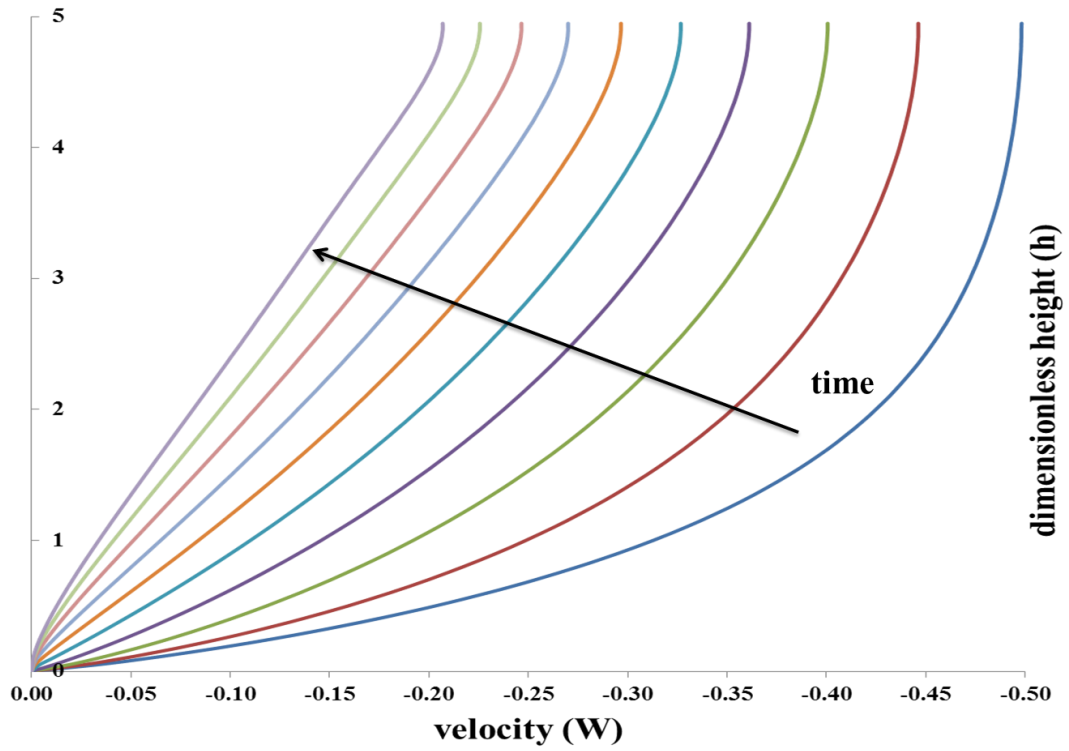


Figure 8: Dimensionless solid velocity vs. dimensionless height in a non-melting Cartesian System. Not that these velocities are negative because the solid moves downward. The separate curves show porosity at ten uniformly spaced times after the initiation of compaction.

Figures 7 & 8 show the evolution of porosity and solid velocity, respectively, for a Cartesian system. The multiple curves on each graph plot the gradual decline of both the porosity and the velocity with time, as the melt is expelled from the top of the column.

Note that **Fig. 2** is a schematic version of **Fig. 7** at very early times.

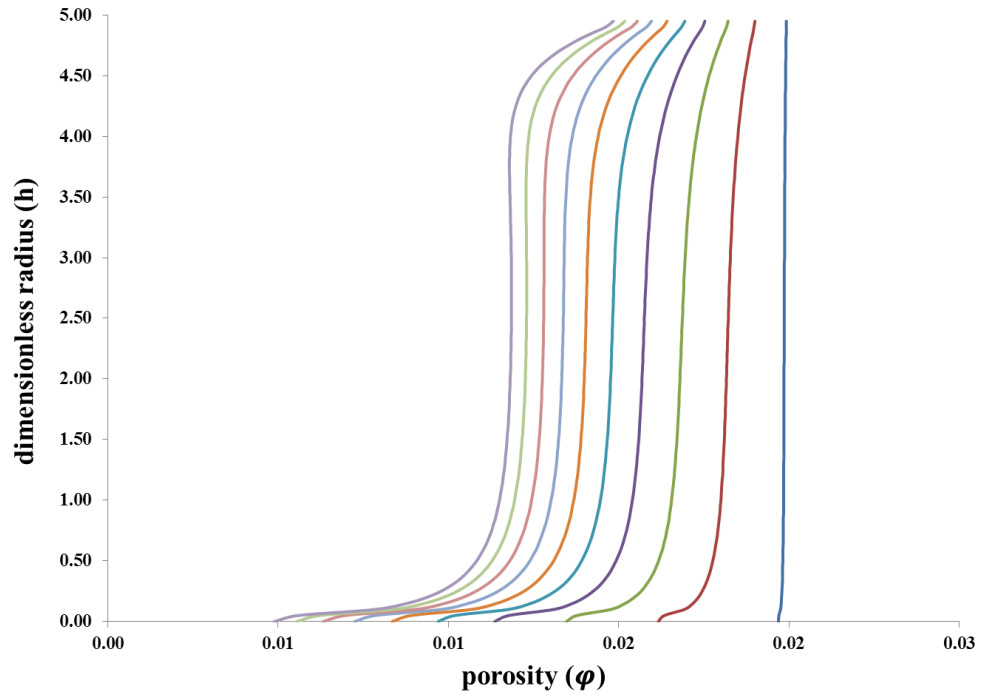


Figure 9: Porosity vs. dimensionless radius in a Spherical system, as in **Fig. 7**.

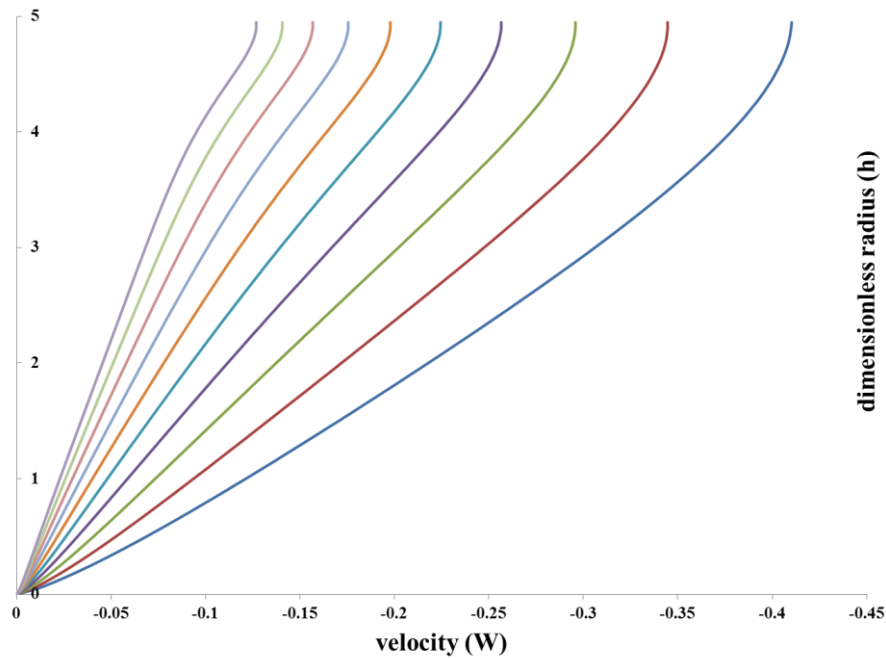


Figure 10: Dimensionless solid velocity vs. the dimensionless radius in a Spherical system, as in **Fig. 8**.

Figures 9 & 10 show porosity and solid velocity in a spherical system. One of the main differences that we can notice is in the porosity graphs. The porosity in the middle of the spherical system is very uniform, whereas in the Cartesian system the porosity increases with height. This is a geometric effect: a volume of melt migrating upward represents a continually smaller fraction of space as it moves into larger outer shells; this counteracts the increase of porosity with height seen in **Fig. 7**. The velocity graphs show us something also. In the spherical system the solid velocity increases nearly linearly with radius, whereas in the cartesian system velocity increases more rapidly with height over the bottom few compaction lengths. This effect is due to gravity: in the spherical

systems the driving force near $r = 0$ is small, so compaction at the center is relatively slow. Despite the difference in distribution of porosity the mean porosity in the two problems is approximately the same, so the melt in spherical problem does not segregate significantly faster or slower.

5. RESULTS FOR MELTING PLANETESIMALS

The evolution of porosity within the melting core depends on two characteristics of the problem, the melting rate scaled by the time scale for porous flow (**Eq. 34**), Γ , and the radius of the melting core scaled by the compaction length scale (**Eq. 35**), h . We have conducted experiments at 5 different values of h and two values of Γ . Each simulation begins with a uniform core composed of 50% ice and 50% rock, by volume. A uniform constant melting rate is imposed over the entire core. Since the two-phase equations break down when the water fraction (porosity) is zero or one, we impose an initial 0.2% porosity, and prevent it from decreasing below this level. Each experiment is run for at least enough time for the ice to completely melt and the water to finish migrating out of the compacted core. Since the core begins at 50% ice, full differentiation will leave a smaller core of rock with a radius $\sim 0.8 R_0$, overlain by a mantle of liquid water.

Below we illustrate two end-member paths: 1) melting faster than migration, which occurs for high melting rates and/or core radii that are only a few compaction lengths, and 2) melting slower than migration, which occurs for low melting rates and/or core radii that are many compaction lengths.

5.1 Endmember 1: Melting Faster than Migration

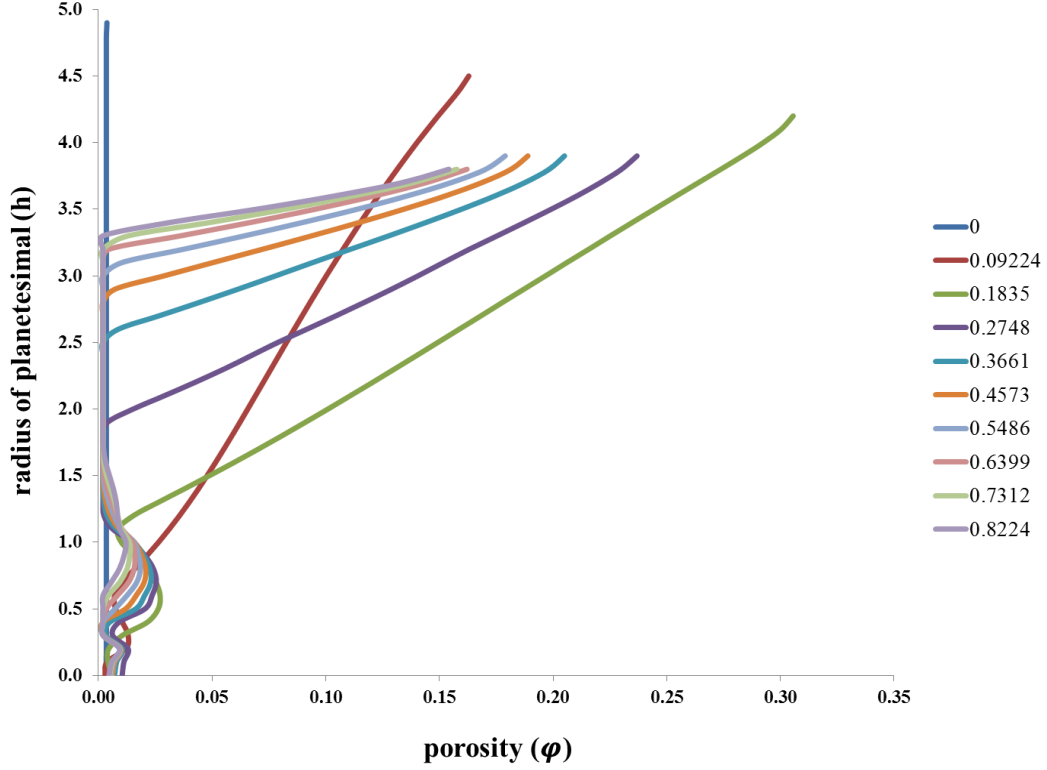


Figure 11: Porosity vs. compaction length with a fast melting value (.86 million years accretion time) and a radius of five compaction lengths. The separate curves show porosity at different dimensionless times.

As an example of the first endmember, we choose a simulation of a melting core that is five compaction lengths in radius ($h = 5$), and has a fast melting rate of $\Gamma = 4.46 \times 10^{-11}$. **Figure 11** shows the evolution over time of porosity vs. radius. At a given time porosity increases nearly linearly with radius, reaching its maximum value at the top of the partially molten region (base of the water layer). The porosity in the entire core quickly grows to large values, peaking at a dimensionless time of about 0.23, when

all ice in the core has melted. After this time, with the source of new meltwater gone, the porosity decreases steadily, as the melt drains out. Porosities become very small at the bottom of the column due to compaction, and some small porosity waves can be seen forming there. The compacted (near melt-free) center of the core grows with time. The mid- and outer levels of the core maintain significant porosity for a longer time. This is because these regions have an influx of water from the entire underlying portion of the core, so these regions take longer to empty of liquid. The position where the top of the porosity curves truncate shows how the water layer thickens over time.

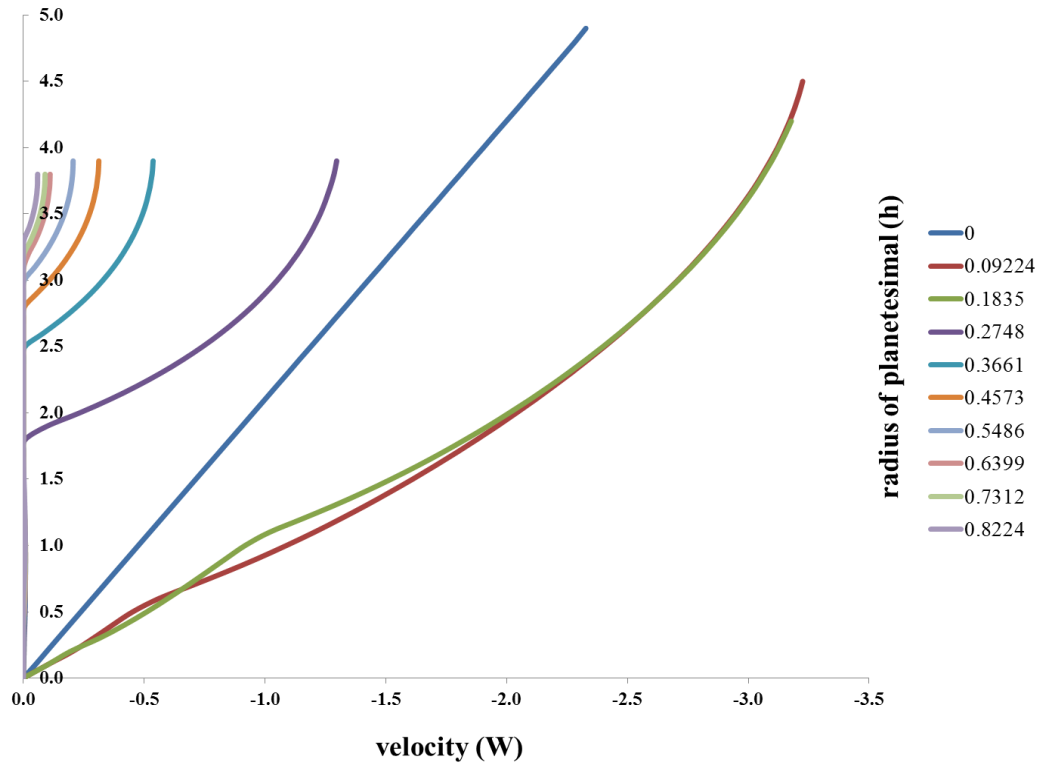


Figure 12: Velocity of solid phase vs. height for the compacting Spherical model shown in **Fig. 11**.

The final porosity curves in **Figure 11** show a narrowing region of still-high porosity beneath the base of the water layer. This region at the top of the core takes a long time to completely compact, because the height of the compacting column has become less than one compaction length, and the velocities have decreased. This is shown by the solid velocity profiles in **Figure 12**. These profiles also reflect the rapid increase and slow decrease in porosity, during and after melting, respectively. Note that the velocity profiles shown here are different from the no-melting simulation shown in the previous section (**Figs. 10**). In the simulation without melting the velocity profiles are more nearly linear with radius from the core than shown in **Figure 12**. While porosity decreases by about a factor of 2 between the end of melting and $t' = 1$, velocity decreases by more than an order of magnitude. This is explained partly by the nonlinear dependence of permeability on porosity, but also partly by the boundary conditions: with zero velocity at the bottom of the compacting column, and zero gradients in the solid flux at the top, the velocities are constrained to be rather small. This accounts for the slow draining of this top layer, even though porosity is more than 0.1. However, we consider the core to be effectively completely drained by a time of 1, because the volume of water in the core is $< 2\%$ of the initial ice volume.

We can track the progress of the segregation of water from the core by the radius of the base of the accumulated shell of water on top, R_w . This radial distance is scaled by the original radius of the melting core, so R_w always begin at 1 (**Figure 13**). The ‘staircase’ nature of this plot is due to rounding R_w to the nearest grid point of the

numerical model. Once melting stops there is drastic slowdown of the growth of the water layer.

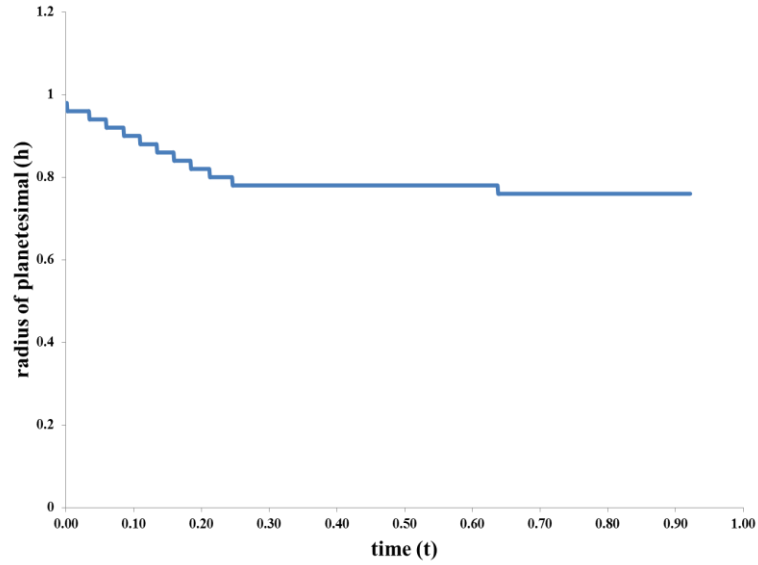


Figure 13: The evolution of the radius of the top of the melting core, scaled by the original size of the core, vs. time for the run with $h = 5$ and $\Gamma' = 4.46 \times 10^{-11}$. The break in slope, at which time almost all of the melt has segregated from the core, is the “end of compaction”.

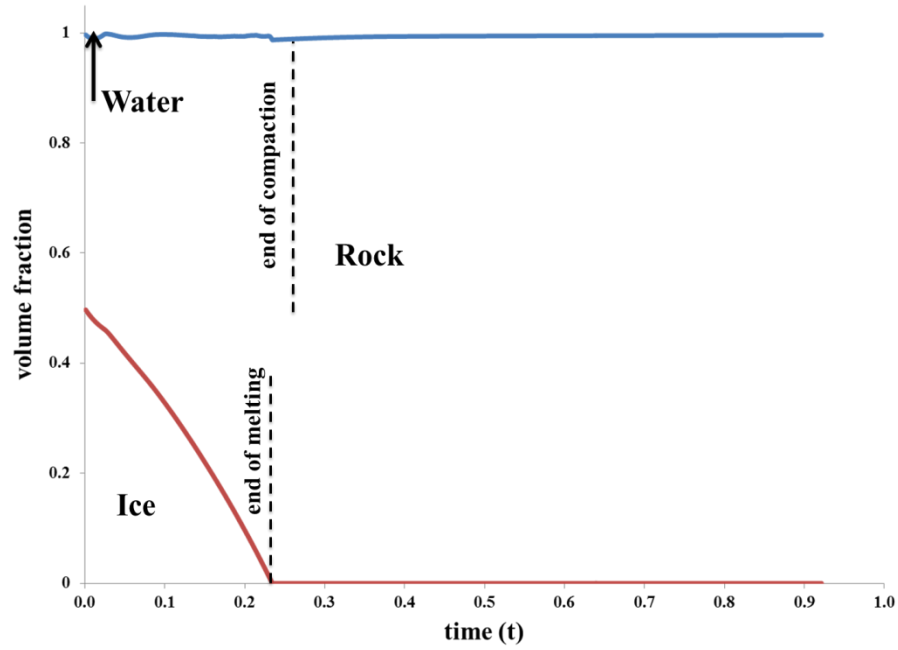


Figure 14: Composition of the melting core (based on volume fraction of ice, rock, and water) vs. time at the center of the core ($r = 0$) for the simulation shown in **Fig. 11 & 12**. The area below the red curve represents the volume fraction of ice, and the area above the blue curve is the volume fraction of water. The area between the two separate curves represents the volume fraction of rock.

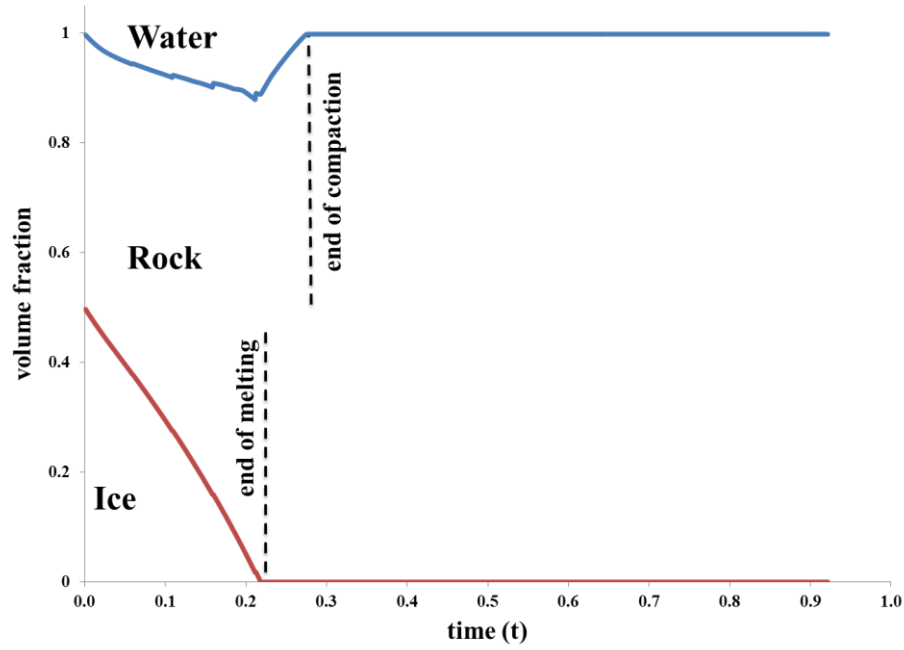


Figure 15: Composition of the melting core (based on volume fraction of ice, rock, and water) vs. time at mid-radius ($r = \frac{h}{2}$) for the simulation shown in **Fig. 11 & 12**. See **Fig. 14** for an explanation of curves.

Figures 14 and 15 represent the composition of the melting core as we progress through time at two different locations of the core (at the center and at the mid-radius, respectively). The curves in these figures show the evolution of the volume fraction of the different components. The small area above the blue line represents the water in that portion of the core. This water is very quickly removed from that portion of the system by being squeezed out. The lower section of the graph shows the reduction of the ice component, while the middle section represents the rock component. As melting progresses, the solid part of the core becomes increasingly rock-rich, until the ice is gone at a dimensionless time of approximately 0.235. At the center (**Fig. 14**), the water fraction never grows above about 2%, since compaction is most effective there.

Higher up in the core (**Fig. 15**), water fraction increases continuously to nearly 15% while melting is occurring, but not as fast as ice fraction is reduced. Therefore water extraction from the core is occurring, but not fast enough to prevent a large increase in porosity. Melting stops at this depth at $t' = 0.21$, or slightly earlier than melting at the core center. That is because the high levels of porosity here reduce the amount of ice to be melted, and we are assuming a fixed mass rate of ice lost per volume. If we take into account the increasing heat source due to the concentration of radiogenic isotopes in the rock fraction, we would expect ice to melt even faster at the middle and outer levels. After melting stops, the water fraction drops as the segregation continues, until a time of 0.27, at which the water has been entirely removed. Note that the lower levels of the core become dry faster than the upper levels, as the fully-compacted region propagates upward (as can be seen from the porosity curves in **Fig. 11**).

5.2 Endmember 2: Melting Slower than Migration

As an example of the second endmember, we choose a simulation with $h = 5$, and a much slower melting rate ($\Gamma' = 6.23 \times 10^{-13}$).

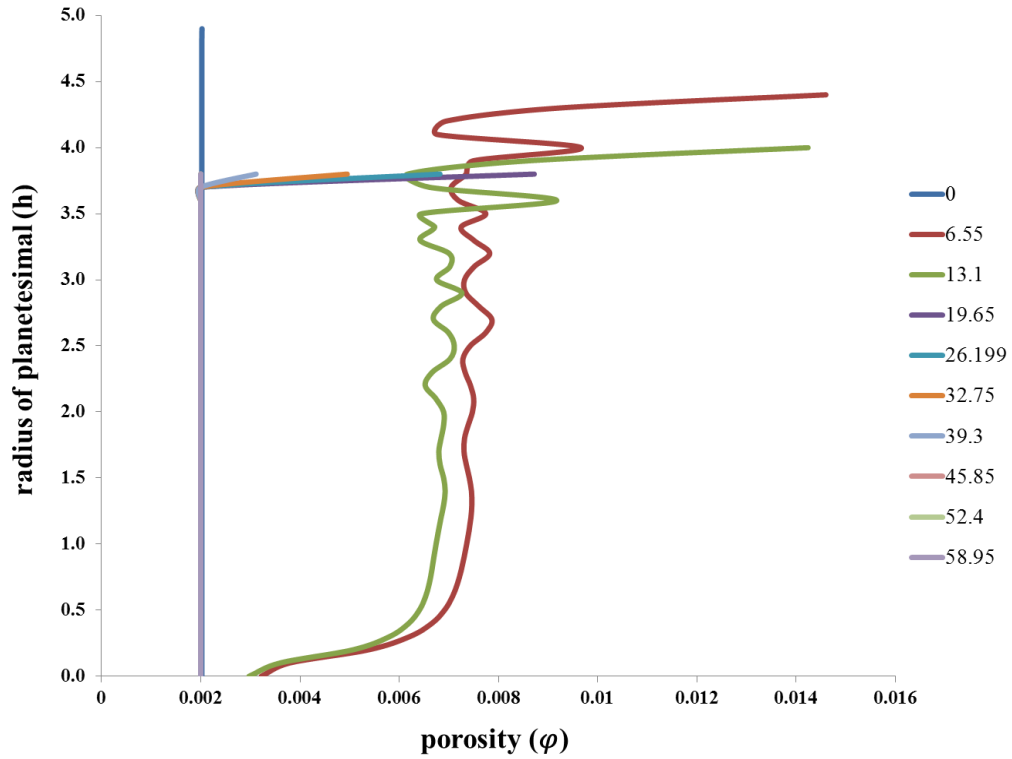


Figure 16: Porosity vs. compaction length with a slow melting value (6.71 million years accretion time) and a melting core with a radius of five compaction lengths. Note that the time intervals between curves is much longer than in **Fig. 10**.

Because the melting rate here (in **Fig. 16**) is about a factor of 80 slower than in Endmember 1, the dimensionless times in this run are much longer than in **Fig. 11**. The main differences we see are that the porosities here are much smaller (notice the scale of the x-axis). This shows us that the melt is extracted nearly as fast as it is created in this system. Except for the compacting bottom and expanding top layer (plus some small porosity waves), the porosity is relatively uniform during melting, porosity drops to zero quickly as the melting ends and the melt is then segregated. As in Endmember 1, there is

a region which is left undrained at the top of the core for a long time, but this region is much smaller than that in **Figure 11**.

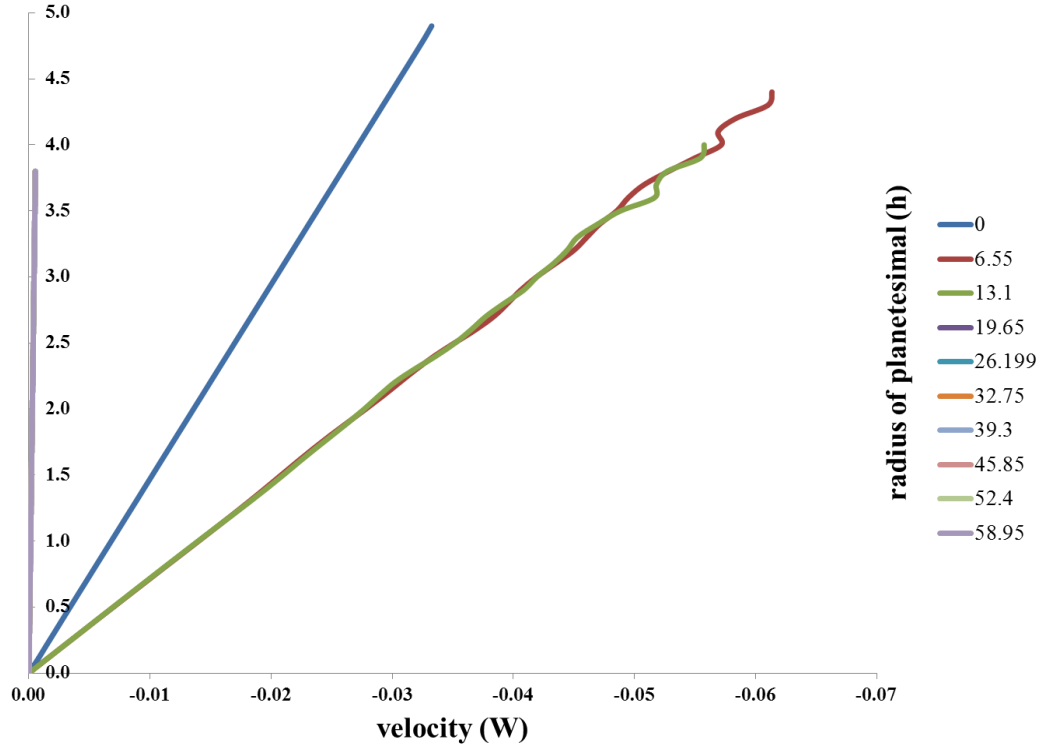


Figure 17: Velocity of the solid matrix vs. the dimensionless radius for the compacting Spherical model from **Fig. 16**.

The solid velocity profiles in this simulation (**Fig. 17**) are drastically different from the Endmember 1 case. Whereas the velocity in the **Fig. 12** had a gradual decline with time that coincided with the slow decrease in porosity, in this case there is an immediate drop in velocity and porosity as soon as melting stops. During melting, the velocity profile is linear with radius, similar to the no-melting simulations (**Figs. 10**).

This is because, with a relatively small value of the melting rate, the system is responding similar to a simple compaction problem, with no melting. The simplest of our models is demonstrated in **Fig. 18**.

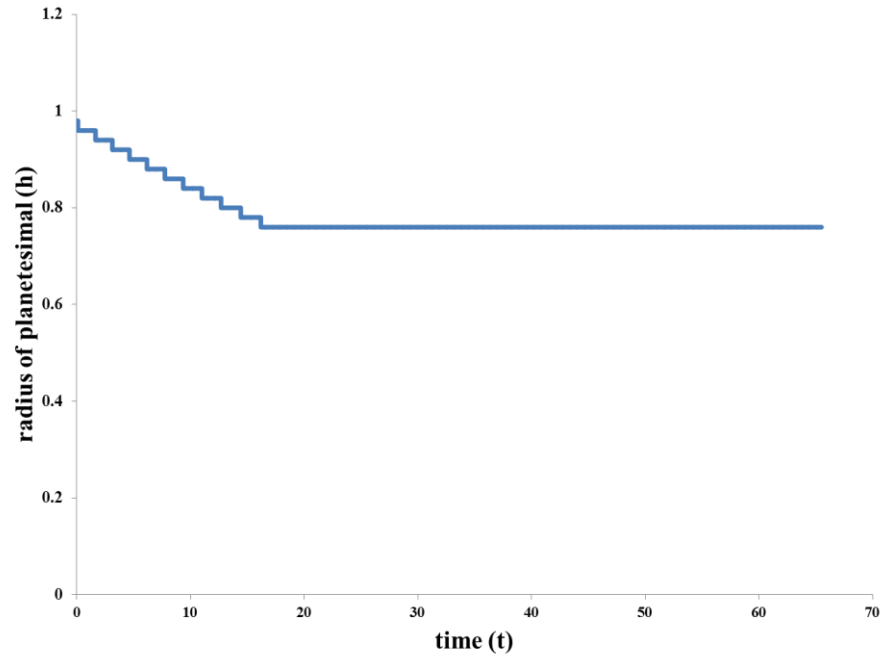


Figure 18: The evolution of the radius of the top of the melting core, scaled by the original size of the core, vs. time for the run with $h = 5$ and $\Gamma' = 6.23 \times 10^{-13}$. The break in slope, at which time almost all of the melt has segregated from the core, is the “end of compaction”.

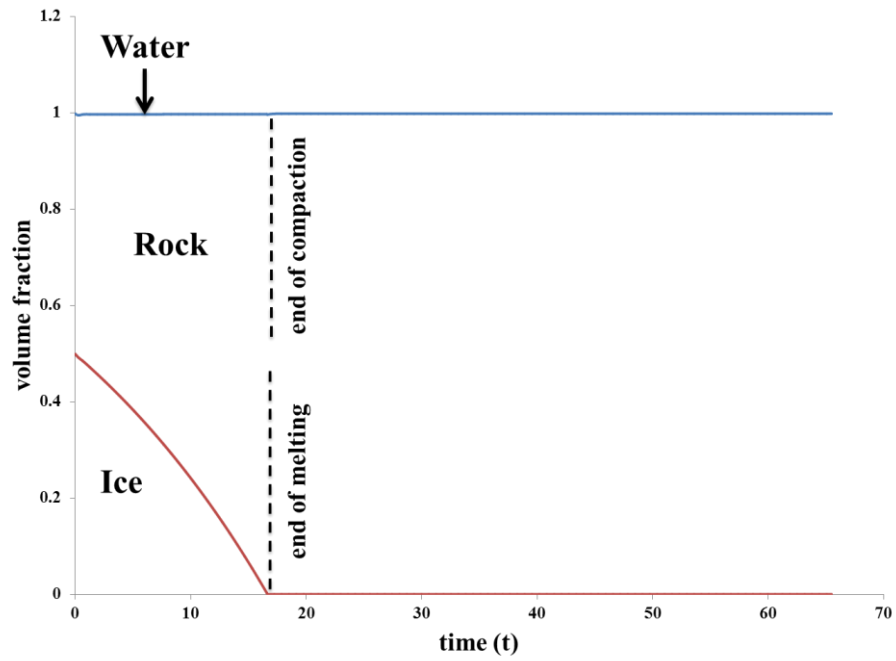


Figure 19: Composition of the melting core (ice, rock, and water) at the center of the planetesimal ($r = 0$) vs. time for the simulation shown in the **Figs. 16 & 17** (melting slower than migration endmember). See **Fig. 13** for description.

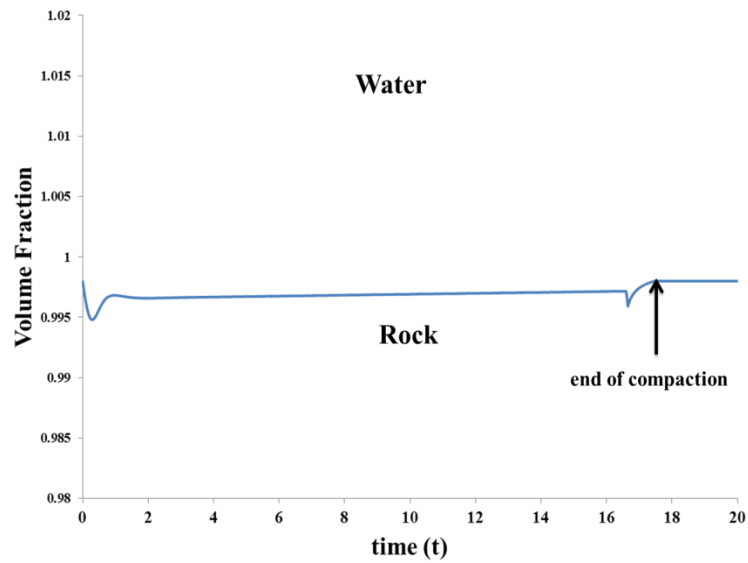


Figure 20: A close up of the water region of **Fig. 19**, showing the small increase in the water fraction before it reverts to ~ 0.002 (which we do not allow to be extracted).

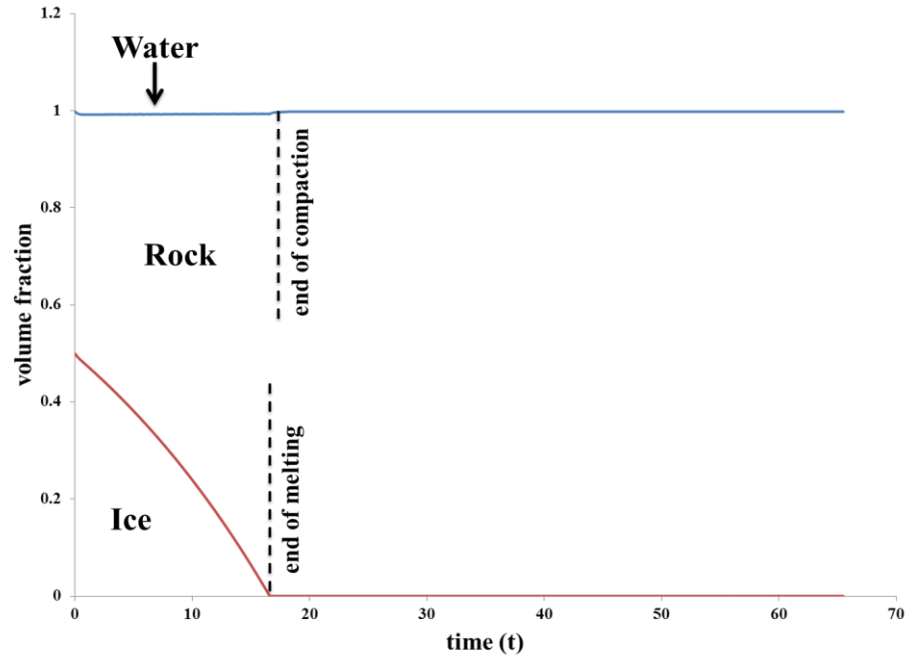


Figure 21: Composition of the melting core (ice, rock, and water) at the $\left(r = \frac{h}{2}\right)$ vs. time for the simulations in **Figs. 16 & 17**.

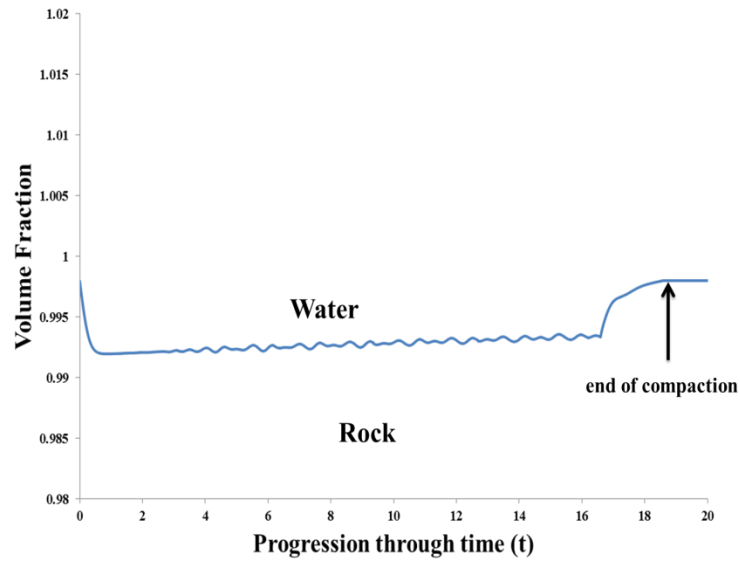


Figure 22: A close up of the water region of **Fig. 21**, showing the small increase in the water fraction before it reverts to ~ 0.002 (which we do not allow to be extracted).

The ice fraction in the second endmember simulation (shown in the **Figs. 19 and 21**) follows a similar pattern as in Endmember 1, except spread over a longer time period. However, the increase in the water fraction during melting is very small, hence the reason for the close-up graphs, **Figs. 20 and 22**. In no portion of the core does the amount of liquid water increase above 1 percent volume fraction. At the center, there is an initial increase to ~0.5% and then a gradual decrease from there to the point at which the water is squeezed out of the core. At the mid-radius of the core, the increase and decay is slightly larger and more gradual.

5.3 Effect of Melting Rate and Size of Core

This section summarizes the results of 10 simulations of melting core with the two melting rates just described, and a range of h values. Larger h corresponds to either a larger core, or smaller compaction length (smaller solid viscosity).

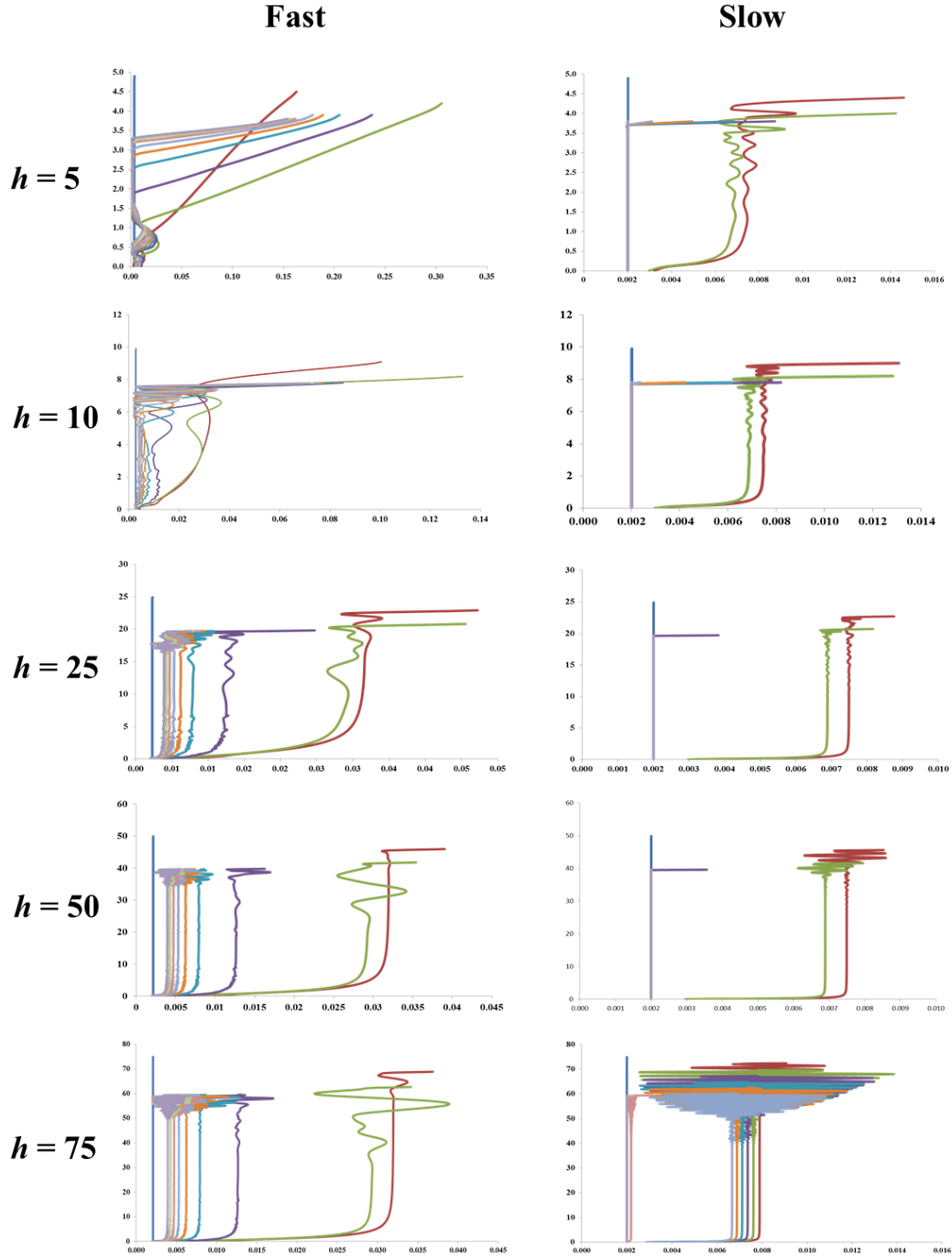


Figure 23: A composite of all of the porosity (x-axis) vs. dimensionless radius (y-axis) graphs for 5 different core size, (h) and two melting rates
 $\Gamma = 4.46 \times 10^{-11} - 6.23 \times 10^{-13}$

Figure 23 shows how the porosity varies as h increases, starting from Endmember 1 (**Fig. 10**) and Endmember 2 (**Fig. 15**). The first end-member (melting faster than migration), can be seen in the left uppermost graph ($h = 5$ in the fast melt column) where the porosity has a rapid increase to a high porosity that varies with radius, and then a gradual decrease extending past the time of melting. In the simulations with higher h , the porosity curves resemble Endmember 2, with melting slower than migration. In these cases, porosity increasing rapidly to a nearly-uniform but small value, then rapidly decays once melting stops. The slight curvature of the porosity curves in a few runs (fast melt, $h = 10$ and 25 , and slow melt, $h = 5$) indicate a transition between these two endmembers, although each of these cases is closer to the second endmember.

For plausible melting rates based on radiogenic heating, any planet core that is larger than $h = 75$ is clearly in the Endmember 2 regime, where migration is significantly faster than the melting rate. As h increases, the porosity during melting stays constant over a larger and larger fraction of core, because the compaction stresses are important only over the bottom few compaction lengths. Because of this we don't stimulate any larger h cores. The porosity waves become very apparent in the high- h simulations: their amplitude grows while the wavelength appears to decrease with increasing h . This is because the wavelength of these waves is approximately the compaction length. The effect of these waves on total extraction time is relatively small however.

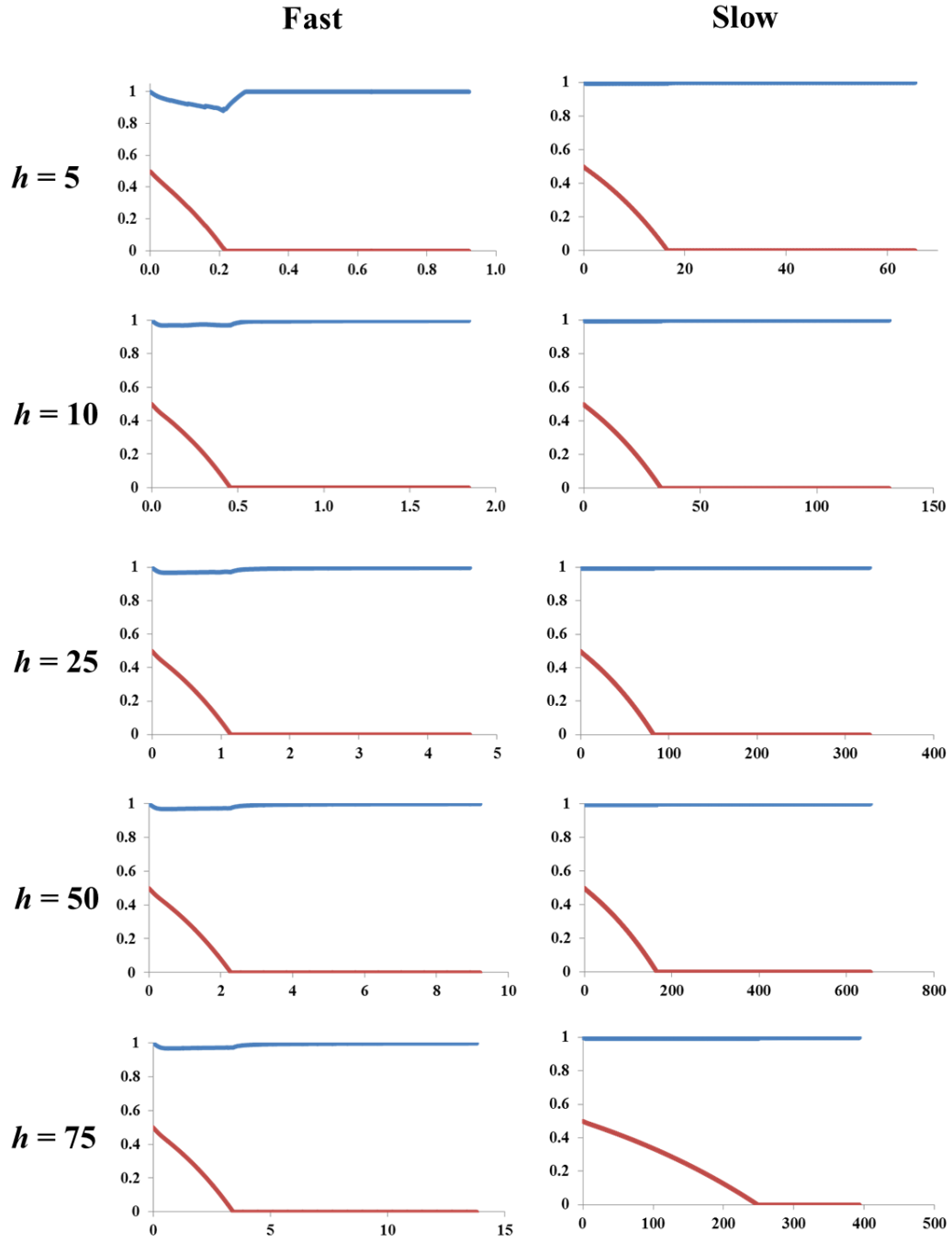


Figure 24: These are the results of the program runs for the composition of the melting core (based on volume fraction of ice, rock, and water) (y-axis) vs. time at $(r = \frac{h}{2})$ (x-axis) for the simulations in **Fig. 23**.

The graphs shown in **Figure 24** are the compositions of the individual planetesimal runs at the mid-radius and the core. The blue curve showing the water content clearly highlights that the Endmember 1 behavior is confined to the smallest, fast melting rate simulation. The red curves show that the dimensionless time for complete melting varies with core size, h . This is due to the fact that the chosen time scale is dependent on gravity, which also varies with core size, and will be discussed in Section 6.

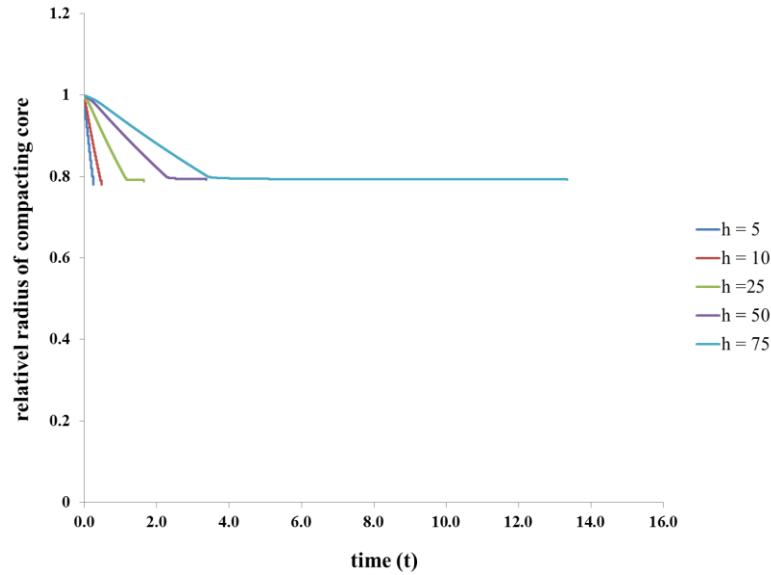


Figure 25: The position of the base of the accumulated water layer, R_w , relative to the original radius of the melting core vs. dimensionless time, for all of the fast melting rate simulations

Figure 25 shows the drop in R_w for all the simulations with the fast melting rate. Given an initial core that is 50% ice by volume, the predicted value of R_w after the core has squeezed out the entirety of the water is ~ 0.779 . In the $h = 5$ simulation, the bulk of

the segregation is completed much faster, by around $t' = 0.23$, although a small amount trickles out for much longer. This graph shows that the time for complete segregation also increases with dimensionless height, similar to the time for complete melting. **Fig. 26** shows a similar relationship in the simulations with the slow melting rate, although all of the times are longer.

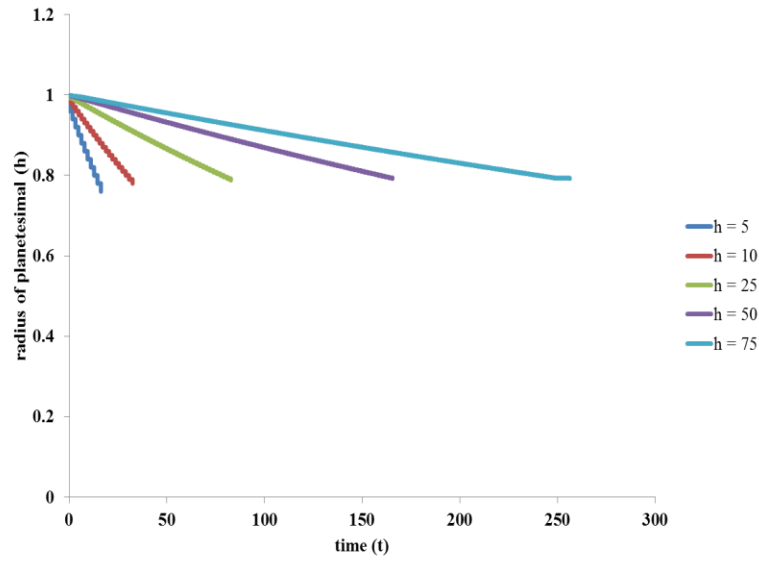


Figure 26: The position of the base of the accumulated water layer, R_w , relative to the original radius of the melting core vs. dimensionless time, for the slower melting rate, and a range of core radii.

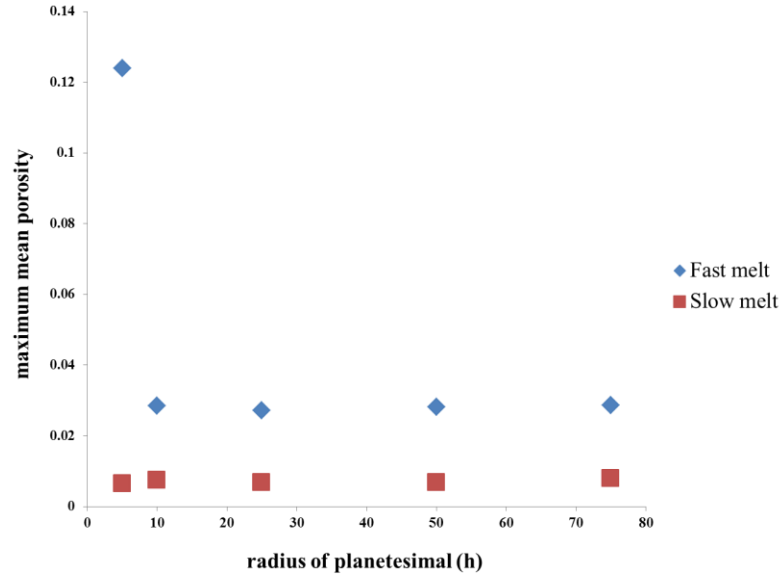


Figure 27: Maximum core-averaged porosity (at different sizes of planetesimals) vs. the dimensionless planetesimal radii.

Figure 27 is a compilation of the core porosity for each simulation. We created this graph by first averaging porosity over the entire core (to remove the effect of porosity waves) at several times in each simulation, then choose the largest of these averages. Nearly all simulations have the same mean porosity as long as they also are given the same melt rate, porosity is not a function of core size, except in the Endmember 1 case.

6. DISCUSSION

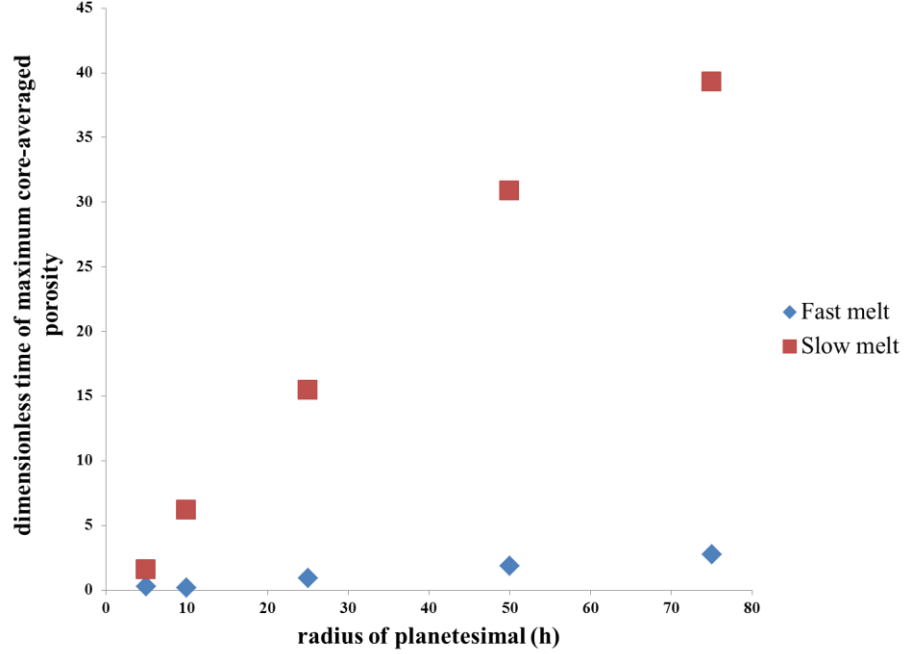


Figure 28: Dimensionless time for complete melting vs. dimensionless core radius.

As was seen in section 5, the dimensionless time for melting and segregation increase with decreasing melting rate and increasing h (dimensionless core radius) [seen in **Fig. 28**]. **Fig. 29 & 30** also show a clear linear dependence on h . This is a surprising result, since the time for melting should not depend on core size. However this effect seen in these figures is a result of the scaling: the time scale depends on h , as will be shown in the following section.

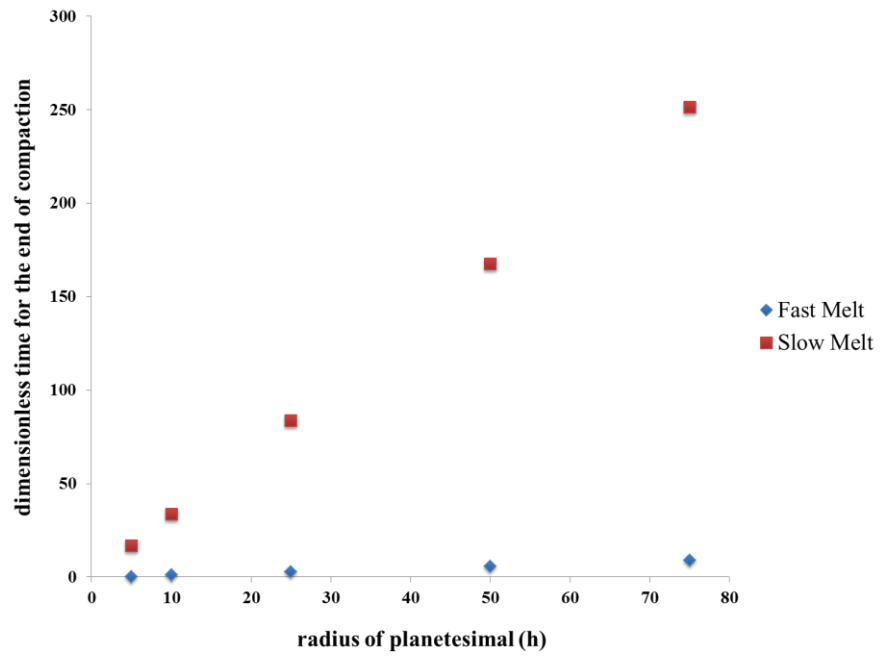


Figure 29: Dimensionless time for core compaction vs. dimensionless core radius.

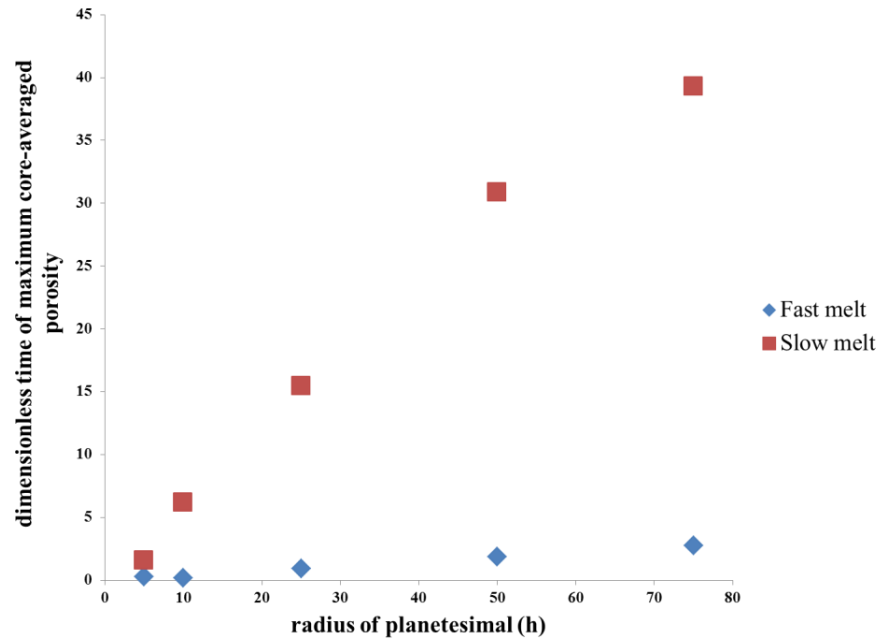


Figure 30: Dimensionless time that the maximum core-averaged porosity (**Fig. 27**) was reached for each run vs. the dimensionless planetesimal radii.

6.1 Large h Approximation

For large- h simulations, the compaction stresses are not very important except in a small layer at the bottom of the core. Therefore, for these situations, we should be able to develop an approximate model that describes the averaged behavior. With no effect from compaction stresses, we can approximate fluid velocity with the Darcy velocity:

$$w_f = \frac{K\Delta\rho g}{\varphi\mu} \quad \text{Eq. 38}$$

The porosity will be dynamically determined by the system to create enough permeability to allow the melt flux at any given radius to equal the total rate of melt production below that radius. We can find that porosity by setting the fluid mass flux passing through a spherical surface of radius r equal to the integrated rate of melting produced within a sphere of radius r .

$$(4\pi r^2)(\rho_f \varphi^* w_f) = \Gamma \left(\frac{4\pi}{3} r^3 \right) \quad \text{Eq. 39}$$

where φ^* is the porosity. Substituting for w_f

$$\frac{\rho_f K^* \Delta\rho g}{\mu} = \Gamma \frac{r}{3}$$

where K^* is the permeability created by the porosity φ^* . Since g varies throughout the layer, we substitute the value for gravity at this radius, along with the expression for permeability

$$\frac{\rho_f \left(\frac{a^2 \varphi^{*3}}{1000} \right) \Delta\rho \left(\frac{4\pi}{3} Gr\rho_s \right)}{2\mu} = \Gamma \frac{r}{3}$$

We can solve this for porosity

$$\varphi^* = \left(\frac{500\mu\Gamma}{a^2\Delta\rho\rho_f\pi G\rho_s} \right)^{1/3} \quad \text{Eq. 40}$$

Note that this porosity is not a function of radius, as is clear in the Endmember 2 cases shown in **Fig. 22** (ignoring areas affected by compaction stresses, including the bottom and top of the region and porosity waves). The mean porosity for the slow melting rates is 0.007, and is 0.03 for the fast melting rates, from **Fig. 26**. Given that the fast melting rate is 71 times larger than the slow melting rates used, **Eq. 40** predicts a difference of a factor of 4.1 in the porosities, which is exactly what is observed in the numerical results.

Substituting this porosity into **Eq. 38** gives

$$w_f = \frac{1}{750} \left(\frac{a^2\Delta\rho\rho_f\pi G}{\mu} \right)^{1/3} \left(\frac{500}{\rho_s} \right)^{2/3} r\Gamma^{2/3} \quad \text{Eq. 41}$$

Combining the various constants in **Eq. 41** into a single variable, θ , we see that melt velocity varies linearly with radius, and increases with the melting rate to the $2/3$ power:

$$w_f = \theta r\Gamma^{2/3}$$

We can now define an approximate “migration time scale” as the time melt takes to cross the upper 90% of the core (to avoid the region at the bottom where compaction stresses are necessary). We define the melt velocity as the rate of change of radial

position, r , with time. $W_f = \frac{dr}{dt}$ Since velocity is a linear function of radius, position of melt at any time within a core of radius R will be given by

$$r = 0.1Re^{\theta\Gamma^{2/3}t}$$

So the time required to cross an entire core of radius R will be given by

$$t_{migrate} = \frac{\ln 10}{\theta \Gamma^{2/3}} \quad \text{Eq. 42}$$

If we compare this extraction time to the time to melt all of the ice in the core (from section 2.3)

$$\frac{t_{migrate}}{t_{melt}} = \frac{\ln 10 / \theta \Gamma^{2/3}}{500 / \Gamma} = \frac{\ln 10}{500 \theta} \Gamma^{1/3}$$

In the simulations, we assumed a grain size of 1 *mm*. Using other values for densities and melt viscosity (see Table 2), $\theta = 3 \times 10^{-6}$. For the slower melting in our simulations this ratio is 0.12. Since the time to get melt out of the core is less than the time or melting the core, this implies that at this melting rate (assuming a core that is many compaction lengths in radius), melt will always get out about as fast as it is created. For the fast melting rate, this ratio is ~ 0.5 , indicating that melt will accumulate somewhat in the core. A melting rate that was 5-10 times faster should overwhelm the ability of the melt to migrate, and large porosities will accumulate.

6.2 Timing of Melting and Segregation

Previous **Figs. 25 – 30** indicated that the time for melting and segregation both depend on melting rate, and dimensionless radius of core. This second dependence is a function of the time scale. Not that the chosen time scale depends on the velocity scale.

$$t_0 = \frac{\delta_c}{W_0}$$

The velocity scale depends on the gravity scale, g_0 , which increases linearly with core radius. Substituting for both g_0 and W_0 :

$$t_0 = \frac{\delta_c}{\frac{K_0}{\mu}(1 - \varphi_0)g_0\Delta\rho_0}$$

$$t_0 = \frac{3}{4\pi} \frac{\delta_c}{G\rho_s R_0(.5(\rho_R + \rho_I) - \rho_w)} = \frac{3}{4\pi G\rho_s R_0(.5(\rho_R + \rho_I) - \rho_w)} \frac{1}{h}$$

Therefore the time scale varies linearly with compaction length divided by core radius, or inversely with h . So while dimensionless melting time varies linearly with h if we convert to dimensional time, the dependence on core size disappears. **Fig. 31** shows real melting times for the simulations, showing that there is no size-dependence.

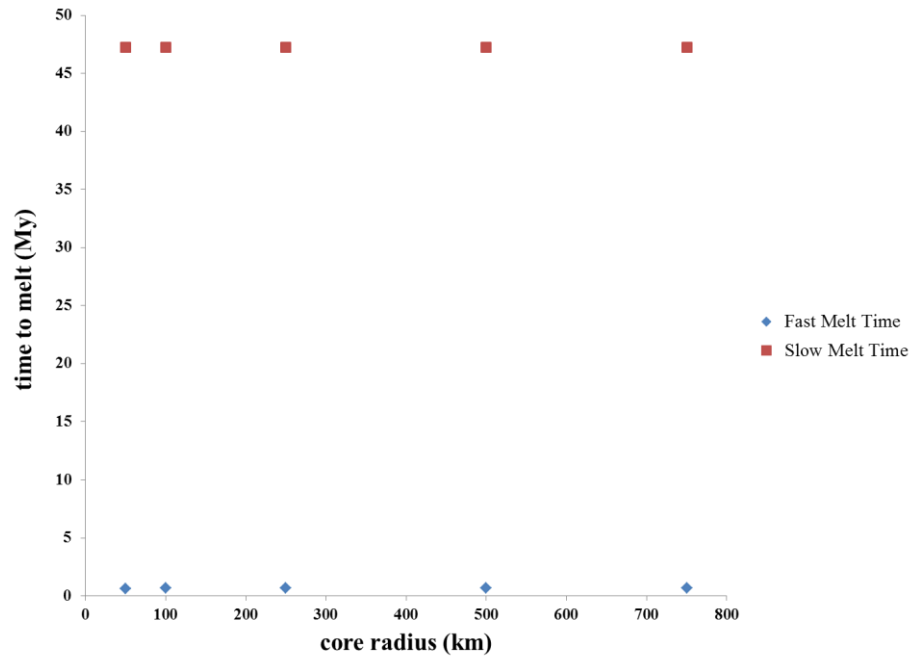


Figure 31: Melting time vs. initial core radius. The conversion to dimensional radius assumes a ratio of solid viscosity to ice viscosity of 10^6 .

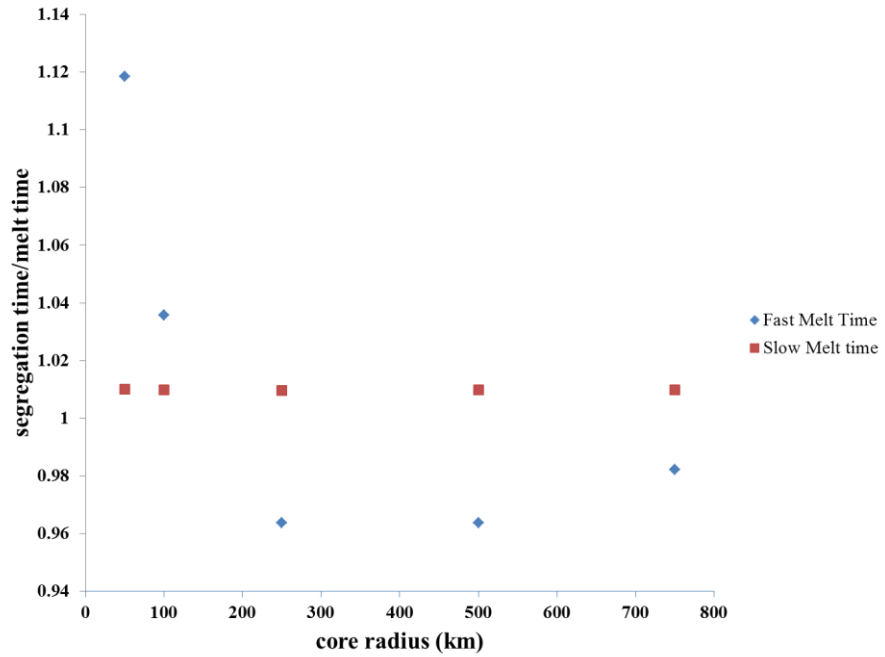


Figure 32: Segregation time/Melt time vs. core radius.

Figure 32 plots the ratio of the time for segregation of melt to the time for complete melting of the core for all of the simulations. In this plot, time to melt is defined as the time when ice at the center of the core has completely vanished. This is slight underestimate of the total melting time, since end of melting propagates upward through the core with time. Segregation time is defined as the time when the rapid growth of the water layer ceases. In some cases, this is a slight underestimate of the time, because a small amount of water ($< 1\%$ of the total) comes out at a much slower rate. In the slow melting cases this ratio is slightly greater than 1, indicating again that melt is coming out of the system as fast as it is created. In the fast melting cases with small $h \leq 10$, the segregation time is 4 to 12% greater than the melting time, because compaction stresses have slowed the migration of melt out of the core. In the larger h cases, the ratio is < 1 because of the slower upward propagation of the end of melting.

7. CONCLUSION

This thesis describes a numerical model of a part of the differentiation history that a small ice/rock planetesimal could experience. To do this we adapted the approach developed by McKenzie for a partially molten upper mantle in the Earth, to a spherical core melting ice mixed with rock. The model is designed to analyze the time necessary for a planetesimal of a given size and melting rate to differentiate into a compacted core of rock overlain by a mantle of water. This time is affected by the gravity-driven buoyancy of the melt, the resistance of the remaining solid core to compaction, and the permeability of the core. This required rederiving McKenzie's formulation in 1-D radial coordinates, accounting for the variable gravity in the core of a planetesimal, and the uncertainties in the viscosity of the ice/rock mixture.

We determined from simple initial models, a small (a few compaction lengths in radius) non-melting bodies, the effects of spherical spreading and variable gravity do not significantly change the total segregation time from a model done with constant gravity in 1-D cartesian coordinates. However, the details of the porosity distribution vs. radius are different in the spherical problem.

From a suite of numerical models, we have determined that under almost all circumstances, the meltwater is segregated out of the core as fast as it is created, and the porosity remains $< 1\%$. In these cases, the melting rate controls the amount of time necessary for a planetesimal to complete its segregation and compaction. In only one model, which we identify as Endmember 1, do we see migration slow enough that the

segregation time is significantly longer than the melting time (0.75 My vs. 0.62 My).

This situation occurred when the core radius was only five compaction lengths (~25 and 150 km, depending on the mean core viscosity), and the melting rate was relatively fast (corresponding to radiogenic decay that contains a fairly high contribution from ^{26}Al), less than 1 My after the beginning of accretion.

The segregation in the Endmember 1 case is slower because of compaction stresses that resist compaction in the small core. This allows production of new melt to overwhelm the migration of melt. However at the slower melting rate we tested, this process does not happen even in our smallest core. Therefore, we surmise whether the core is melting-dominated or migration-dominated depends strongly on core size in compaction lengths, but also weakly on melting rate, and predict that at faster melting rates than the one we tested, we would expect the Endmember 1 behavior to extend to larger cores. Much larger melting rates due to radiogenic heating might be unlikely, but if we were to add in the contribution of serpentinization, the melting rates could be much higher.

Most of our models indicate that migration is very fast, so the meltwater does not stay long in the core, which could inhibit serpentinization. However, any serpentinization will tend to drive up melting rates, and create higher water fractions in the core, which should help to drive the reaction. Therefore, our model indicates that if the water-rock reaction can begin, it will overwhelm migration and lead to a water-rock core which can then react while compacting out any excess fluid. A careful study of the

kinetics of the water-rock reaction, in conjunction with these models is necessary to better determine the evolutionary path of most ice-rock planetesimals.

REFERENCES

- Asimow, P.D., 2002. Steady-state Mantle-Melt Interactions in One Dimension: II. Thermal Interactions and Irreversible Terms. *Journal of Petrology*, **43**, num. 9, 1707-1724.
- Bennett, K. A., 2001. Planetary science: Uncool Callisto. *Nature*, **412**, 395-396.
- Brush, S.G., 1977. The Origin of the Planetesimal Theory. *Origins of Life*, **8**, 3-6.
- Choi, C. Q., 2006. Cold Faithful. *Scientific American*, **294**, 29.
- Consolmagno, G.J., 1983. Ice-Rich Moons and the Physical Properties of Ice. *Journal of Physical Chemistry*, **87**, 4204-4208.
- Consolmagno, G.J. & Lewis, J.S., 1978. The Evolution of Icy Satellite Interiors and Surfaces. *Icarus*, **34**, 280-293.
- De Sanctis, M. C., Capria, M. T., and Coradini, A., 2001. Thermal Evolution and Differentiation of Edgeworth-Kuiper Belt Objects. *The Astronomical Journal*, **121**, 2792-99.
- Elkins-Tanton, L.T., Weiss, B.P., and Zuber, M. T., 2011. Chondrites as samples of differentiated planetesimals. *Earth and Planetary Science Letters*, **305**, 1-10.
- Farrell, L., McGary, S. and Sparks, D.W. 2007. Thermal history and differentiation of ice/rock planetesimals, *Lunar and Planetary Science Conference*. **39**, 1-5.
- Gurnett, D., Kurth, W.S., Roux, A., Bolton, S.J. & Kennel, C.F., 1996. Evidence for a magnetosphere at Ganymede from plasma-wave observations by the Galileo spacecraft. *Nature*, **384**, 535 – 537.
- Johnson, T.V., 2004. Geology of Icy Satellites. *Space Science Reviews*, **116**, 401-420.
- Kerr, R. A., 2012. Cassini spies an Ocean Inside Saturn's Icy, Gassy Moon Titan. *Science*, **336**, Iss. 6089, 1629.
- Mader, H.M., 1992. Observations of the water-vein system in polycrystalline ice. *Journal of Glaciology*, **38**, no. 130, 333-347.

- Malvoisin, B. et al., 2012. Serpentinization of oceanic peridotites: 2 Kinetics and processes of San Carlos olivine hydrothermal alteration. *Journal of Geophysical Research*, **117**, B04102, 13.
- McCord, T.B. and Sotin, C., 2005. Ceres: Evolution and current state. *Journal of Geophysical Research*, **110**, E05009.
- McKenzie, D., 1984. The Generation and Compaction of Partially Molten Rock. *Journal of Petrology*, **25**, pt. 3, 713-765.
- Merk, R. and Prialnik, D., 2006. Combined modeling of thermal evolution and accretion of trans-Neptunian objects—Occurrence of high temperatures and liquid water. *Icarus*, **183**, 283-295.
- Merk, R. and Prialnik, D., 2003. Early thermal and structural evolution of small bodies in the trans-Neptunian zone. *Earth, Moon, and Planets*, **92**, 359-374.
- Nian-Sheng, C. & Wing-Keung Law, A., 2003. Exponential Formula for computing Effective Viscosity. *Powder Technology*, **129** (1-3), 156-160.
- Prialnik, D., and Bar-Nun, A., 1989. Heating and Melting of Small Icy Satellites by the Decay of ²⁶Al. *The Astrophysical Journal*, **355**, 281-86.
- Rabinowicz, M. and Toplis, M., 2009. Melt segregation in the Lower part of the Partially Molten mantle zone beneath an Oceanic Spreading Centre: Numerical Modeling of the Combined Effects of shear segregation and compaction. *Journal of Petrology*, **50**, num. 6, 1071-1106.
- Ribe, N., 1985a. The deformation and compaction of partial molten zone. *Geophysics. J. R. Astronomy. Soc.*, **83**, 487-501.
- Ribe, N., 1985b. The generation and composition of partial melts in the Earth's mantle. *Earth and Planetary Science Letter*, **73**, 361-376.
- Richter, F., and McKenzie, D., 1984. Dynamical models for melt segregation from a Deformable Matrix. *Journal of Geology*, **92**, 729-740.
- Scott, D. R., and Stevenson, D. J., 1986. Magma ascents by porous flow. *Journal of Geophysical Research*, **91**, NO. B9, 9283.
- Sohl, F., 2010. Interior Models of Icy Satellites and Prospects of investigation. *International Astronomical Union*, **263**, 113-120.

Sohl, F. et al., 2010. Subsurface Water oceans on Icy Satellites: Chemical Composition and Exchange processes. *Space Science Review*, **153**, 485-510.

Spiegelman, M., 1993a. Flow in Deformable porous media: Part 1 Simple analysis. *Journal of Fluid Mechanics*, **247**, 17-38.

Spiegelman, M. , 1993b. Flow in deformable porous media: Part 2 Numerical analysis – the relationship between shock waves and solitary waves. *Journal of Fluid Mechanics*, **247**, 39-63.

Wilson, L., Keil, K., and Love, S.J., 1999. The internal structures and densities of asteroids. *Meteorites and Planetary Science*, **34**, 479-483.

APPENDIX 1

Finite Difference Fortran program for Melting and Migration in Spherical Coordinate system

```
INTEGER N, M, jcount, Wp
PARAMETER (Nmax = 18501)
PARAMETER (Maxsteps = 300000)
REAL*8 dtfactor, h, p0, pfl, pso, con,spf
REAL*8 dr, dtmax, xp, dt, dep
REAL*8 W(Nmax), v(Nmax), p(Nmax), ps(Nmax), rf(Nmax), f(Nmax),
1      res(Nmax), psn(Nmax), r(Nmax), S(Nmax), si(Nmax), z(Nmax),
1      g(Nmax), Y(Nmax), X(Nmax), gr(Nmax), ep(Nmax), vis(Nmax),
1      phip(Nmax), rhs(Nmax), Melt(Nmax), Melt0, vis0(Nmax),
1      delp(Nmax), psolid(Nmax)
REAL*8 xi(Nmax),xin(Nmax),xr(Nmax),xrn(Nmax)
REAL*8 pice,rock0, prock, K, mew
REAL*8 pi, avp, Gravity, Me, Mmelt
REAL*8 rest(100*Nmax), Wtop(100*Nmax)
REAL*8 rm(Maxsteps)
REAL*8 incp(Nmax,10), incW(Nmax,10), inci(Nmax,10)
REAL*8 incr(Nmax,10), incps(Nmax,10)

      read(*,*) h, N, Metype, ibetatype
c    N=801
      ibot=1
      dtfactor = 0.01
c    h = 150.0
      dr = h/(N-1)
      p0 = 0.02
      psmx=1./p0
      rock0=0.5
      pfl = 1000.
      pice=920.
      prock=3300
      pso = 2000.
      dep = (pso-pfl)
      K = 8.e-15
      mew = 1e-3
      pi = 4*atan(1.0)
      avp = 2000.
```

```

Gravity = .667e-10
if (Metype .eq. 1) then
  Me = 4.458e-11
else if (Metype .eq. 2) then
  Me = 2.66e-12
else
  Me = 6.27e-13
endif

```

```

if (ibetatype .eq. 1) then
  beta = 1.6
else
  beta = 2.5
endif

```

```

print*, h, N, Me, beta

```

c Scale the melting rate; time scale depends on h.

```

Melt0 = (Me*mew)/(h*pfl*K*(1-p0)*dep*(4/3)*pi*avp*Gravity)
print*, Melt0

```

```

con = 5./7.

```

c if spf=2., this is the spherical equation (this program only does cartesian now)
 spf=2.

```

open(unit=15,file="vis.txt")

```

```

DO      i = 1, N
  if (spf .eq. 2.) then
    gr(i) = float(i-1)/float(N-1)
  else
    gr(i) = 1.
  endif
  Melt(i) = Melt0
END DO

```

```

R(1)=0.
DO      i = 2, N
  R(i) = dr*float(i-1)
END DO

```

```

DO      i = 1, N
  W(i) = 0.0

```

```

                                v(i) = 0.0
                                p(i) = 0.1
                                ps(i) = (1.-p0*p(i))
                                xr(i)=rock0*ps(i)
                                xi(i)=(1-rock0)*ps(i)

                                psolid(i) = ((pice*xi(i))+(prock*xr(i)))
1                                /( xi(i)+xr(i) )
                                delp(i)=1.

                                END DO

dtmax = (dr*(1-p0))/(1+p0)
dt = dtfactor*dtmax
xp = 3.0
rm(1) = (N-1)*dr
Mmelt = 0.5/(dt*Melt0)

print*, 'Mmelt = ', Mmelt

M = nint(5*Mmelt)
jcount = 0
N0=N

                                open(unit=9, file='xbeginning.txt')
                                open(unit=10, file='xmid.txt')
                                open(unit=11, file='xwater.txt')

                                print*, 'melt=',Melt(1)
Ntop=N
ibot=1

c %%%%%%%%% BEGIN TIME STEPPING LOOP %%%%%%%%%
DO j = 1, M
    tau = j*dt
    vissum=0.
    xrmin=1.
    xrave=0.
    pave=0.
    nvpts=0
do i=ibot,N-1
    if (xr(i) .lt. 1.) then
        pave=pave+p0*p(i)
        xrave = xrave +(xr(i)/ps(i))
        nvpts=nvpts+1

```



```
endif
enddo
```

```

if (nvpts .gt. 0) then
    xrave = min(.75,xrave/float(nvpts))
    pave=pave/float(nvpts)
else
    xrave = .75
    pave=p0*p(N
endif

```

visum=1.

```
do i=1,N
    vis(i)=vissum
enddo
```

```
write(15,*) tau, vis(1), xrave, pave
```

```
write(29,*) xr(1),xr(2),xr(3), ibot
```

```

if (ibot .lt. N-1) then

```

```
DO i=1,ibot
  W(i)=0.
```

ENDDO

DO i = ibot+1, N

```

rf(i) = -2./(dr*dr)
1      -1./(vis(i)*(p(i)**xp))
1      -(spf*con)/(r(i)*r(i))

```

$$f(i) = (1 - p_{fl}/p_{solid}(i)) * ((1 - p_0 * p(i))^* gr(i) / (1 - p_0) + r(i) * Melt(i) / (3 * (p(i)**x_p))) / vis(i)$$

END DO

```
c &&&&&&&&&&& BEGIN ITERATION LOOP&&&&&&&&&&&
```

$$\text{itermax}=30*N0$$

```
DO      iter = 1, itermax
```

DO i = ibot+1,N-1


```

wsp=0.5*(W(i)+W(i+1))
wsm=0.5*(W(i)+W(i-1))
psn(i) = ps(i)+ dt*( -(ps(i+1)*wsp-ps(i)*wsm)/(dr)
1          - spf*W(i)*ps(i)/r(i) )
1          - dt*pfl*Melt(i)/pice

xrn(i) = xr(i)+ dt*( -(xr(i+1)*wsp-xr(i)*wsm)/(dr)
1          - spf*W(i)*xr(i)/r(i) )

END DO
wsm=0.5*(W(N)+W(N-1))
psn(N) = ps(N)-dt*((ps(N)*W(N)-ps(N)*wsm)/dr)
1          - dt* spf*W(N)*ps(N)/r(N)
1          - dt*pfl*Melt(N)/pice

xrn(N) = xr(N)-dt*((xr(N)*W(N)-xr(N)*wsm)/dr)
1          - dt* spf*W(N)*xr(N)/r(N)

DO i = 1, N
    ps(i)=psn(i)
    xr(i)=xrn(i)
c do not system be compressed to zero porosity
    if (ps(i) .gt. 0.998) then
        xr(i)=xr(i)-(ps(i)-.998)
        ps(i)=0.998
    endif

c don't let rock fraction go above 0.7
    if (xr(i) .gt. 0.998) then
        xr(i)=0.998
    endif

c ice fraction
    xi(i)=ps(i)-xr(i)
    if (xi(i) .lt. 0.) then
        xi(i)=0.
        if ((i.eq.1).and.(Melt(i).gt.0.)) then
            print*, 'bottome done melting'
        endif
        Melt(i)=0.
    endif

c finally, get water fraction, and recalculate solid density and delta-rho

```

```

1
      p(i) = (1.-ps(i))/p0
      psolid(i) = ((pice*xi(i))+(prock*xr(i)))
                  /( xi(i)+xr(i) )

      delp(i)=(psolid(i)-pf)/(0.5*(prock+pice)-pf)
END DO

xrave=0.
do i=1,N
  xrave=xrave+xr(i)
enddo

xrave=xrave/float(N)

rc=h*(0.5/xrave)**(1./3.)
Ntop=int(rc/dr)
if (N .gt. Ntop) then
  print*, j, tau, ibot, ' Top =', Ntop
  N=Ntop
endif

increment=M/10

IF (mod((j-1),increment) == 0) THEN
  time = dt*(j-1)
  print*, j, tau,'iterations = ',iter

  jcount = jcount + 1
  IF (jcount .LE. 10) THEN
    DO i= 1,N
      incp(i,jcount)= p0*p(i)
    END DO
    DO i= 1,N
      incps(i,jcount)= ps(i)
    END DO
    DO i= 1,N
      inci(i,jcount)= xi(i)
    END DO
    DO i= 1,N
      incr(i,jcount)= xr(i)
    END DO
    DO i = 1, N
      incW(i,jcount)=W(i)

```

```

                                END DO
                                END IF
                                END IF
                                write(9,*) tau, xr(1), xi(1), p0*p(1)
                                write(10,*) tau, xr(N/2), xi(N/2), p0*p(N/2)
                                write(11,*) tau, r(N)/r(N0), ibot
                                END DO
c  %%%%%%%%%% END TIME STEPPING LOOP %%%%%%%%%%

                                open(unit=7, file='rockfraction.txt')
                                DO i = 1, N0
                                    write(7,300) r(i), (incr(i,jp),jp=1,min(jcount,10))
                                END DO
                                open(unit=7, file='icefraction.txt')
                                DO i = 1, N0
                                    write(7,300) r(i), (inci(i,jp),jp=1,min(jcount,10))
                                END DO
                                open(unit=7, file='solidfraction.txt')
                                DO i = 1, N0
                                    write(7,300) r(i), (incps(i,jp),jp=1,min(jcount,10))
                                END DO
                                open(unit=7, file='porosity.txt')
                                DO i = 1, N0
                                    write(7,300) r(i), (incp(i,jp),jp=1,min(jcount,10))
                                END DO
                                open(unit=8, file='velocity.txt')
                                DO i = 1, N0
                                    write(8,300) r(i), (incw(i,Wp),Wp=1,min(jcount,10))
                                END DO
300  format(11(E13.4,1x))
                                print*, 'melt=',Melt(1)
                                END
                                REAL*8 FUNCTION rNORM1(F,ibot,N)
                                REAL*8 F(N),sum
                                sum=0.
                                DO i=ibot+1,N-1
c  print*, 'F=', F(i)
                                    sum=sum+F(i)**2
                                ENDDO
                                rnorm1=sqrt(sum)
c  print*, rnorm1

                                RETURN
                                END

```